

## A Revised Land Surface Parameterization (SiB2) for GCMs. Part III: The Greening of the Colorado State University General Circulation Model

D. A. RANDALL, D. A. DAZLICH, C. ZHANG, AND A. S. DENNING

*Department of Atmospheric Science, Colorado State University, Fort Collins, Colorado*

P. J. SELLERS, C. J. TUCKER, AND L. BOUNOUA

*Laboratory for Atmospheres, NASA Goddard Space Flight Center, Greenbelt, Maryland*

J. A. BERRY, G. J. COLLATZ,\* AND C. B. FIELD

*Carnegie Institution of Washington, Stanford University, Palo Alto, California*

S. O. LOS AND C. O. JUSTICE

*Department of Geography, University of Maryland, College Park, Maryland*

I. FUNG

*School of Earth of Ocean Sciences, University of Victoria, British Columbia, Canada*

(Manuscript received 23 June 1994, in final form 1 August 1995)

### ABSTRACT

SiB2, the second-generation land-surface parameterization developed by Sellers et al., has been incorporated into the Colorado State University general circulation model and tested in multidecade simulations. The control run uses a "bucket" hydrology but employs the same surface albedo and surface roughness distributions as the SiB2 run.

Results show that SiB2 leads to a general warming of the continents, as evidenced in the ground temperature, surface air temperature, and boundary-layer-mean potential temperature. The surface sensible heat flux increases and the latent heat flux decreases. This warming occurs virtually everywhere but is most spectacular over Siberia in winter.

Precipitation generally decreases over land but increases in the monsoon regions, especially the Amazon basin in January and equatorial Africa and Southeast Asia in July. Evaporation decreases considerably, especially in dry regions such as the Sahara. The excess of precipitation over evaporation increases in the monsoon regions.

The precipitable water (vertically integrated water vapor content) generally decreases over land but increases in the monsoon regions. The mixing ratio of the boundary-layer air decreases over nearly all continental areas, however, including the monsoon regions. The average (composite) maximum boundary-layer depth over the diurnal cycle increases in the monsoon regions, as does the average PBL turbulence kinetic energy. The average boundary-layer wind speed also increases over most continental regions.

Groundwater content generally increases in rainy regions and decreases in dry regions, so that SiB2 has a tendency to increase its spatial variability. SiB2 leads to a general reduction of cloudiness over land. The net surface longwave cooling of the surface increases quite dramatically over land, in accordance with the increased surface temperatures and decreased cloudiness. The solar radiation absorbed at the ground also increases.

SiB2 has modest effects on the simulated general circulation of the atmosphere. Its most important impacts on the model are to improve the simulations of surface temperature and snow cover and to enable the simulation of the net rate of terrestrial carbon assimilation.

### 1. Introduction

As reviewed by Sellers et al. (1996a, hereafter Part I), the importance of land-surface processes for climate

has been increasingly recognized by the global modeling community over the past decade (e.g., Dickinson 1983; Mintz 1984; Sellers et al. 1986; Dickinson et al. 1986; see Garratt 1993 for a review). Among the most obvious motivations for including a realistic land-surface parameterization in a climate model is the need to realistically simulate the flow of moisture between the soil and the atmosphere; this flow is controlled by plants, which act as "solar-powered water pumps," removing moisture from the root-accessible layer of the soil and allowing it to flow out through their stomates

---

\* *Current affiliation:* Laboratory for Atmospheres, NASA Goddard Space Flight Center, Greenbelt, Maryland.

---

*Corresponding author address:* Dr. David A. Randall, Department of Atmospheric Science, University of Colorado, Fort Collins, CO 80523.

even as carbon dioxide flows in through the stomates to be assimilated during photosynthesis. The rate at which water vapor is lost through the stomates is, therefore, determined by the rate of carbon assimilation, which in turn depends on available solar radiation, leaf area, soil moisture, and above all on the biophysical mechanisms through which the plants do photosynthesis.

This paper reports results of a project to incorporate the Simple Biosphere Model (SiB) into the Colorado State University (CSU) general circulation model (GCM). Our project began in 1986 with an effort to couple the UCLA/GLA GCM, then in use at NASA's Goddard Space Flight Center, with the first version of SiB, hereafter referred to as SiB1, which was described by Sellers et al. (1986). Although the coupling itself went smoothly, the results obtained were never very realistic and were not published. Sato et al. (1989a) reported the considerably more satisfactory results obtained in coupling the first version of SiB with the National Center for Environmental Prediction global spectral model, then in use at the University of Maryland. We persevered despite the initially discouraging results with the UCLA/GLA GCM, and after eight years of effort we have finally produced what we consider to be interesting and successful climate simulations with the second-generation version of SiB, called SiB2 (described in Part I), which we have coupled with the CSU GCM derived from the now-defunct UCLA/GLA GCM.

Part I of this series of papers fully describes the formulation of SiB2. Part II (Sellers et al. 1996b) explains how satellite data can be used with the model. The purpose of the present paper, that is, Part III, is to describe our climate simulation results in some detail. The results obtained with SiB2 are compared with observations and also with results of a control run in which the GCM was coupled with a "bucket" hydrology but with the same distributions of surface albedo and surface roughness as those used by SiB2. The differences between the two runs are therefore due to differences in physical formulation and are not due to boundary condition changes. Both runs are ten years long. This makes the differences between them reliable and also allows us to watch the adjustment of the SiB2 version of the model towards its own climatology, including its preferred distribution of soil moisture, which takes several simulated years to become established.

## 2. Description of the model

### *a. The Colorado State University GCM*

The CSU GCM is a child of the UCLA GCM, which was developed at UCLA over a period of 20 years by Arakawa and collaborators. A copy of the model was brought to the Goddard Laboratory for Atmospheres in 1982, and from there to CSU in 1988. Many changes have been made since the model left UCLA. The most important of these are revised solar and terrestrial ra-

diation parameterizations (Harshvardhan et al. 1987), an improved parameterization of cumulus convection (Randall and Pan 1993), and the new parameterization of land-surface processes described in this paper. Additional model development work is in progress.

Some recent results produced with the model are presented by Randall et al. (1985, 1989, 1991), Harshvardhan et al. (1989), and Stephens et al. (1993).

The prognostic variables of the GCM are potential temperature, the mixing ratio of water vapor, the horizontal wind components, the surface pressure, the planetary boundary-layer's depth and turbulence kinetic energy, the ground temperature and snow depth at land points, and the ice temperature at land- and sea-ice points. The governing equations are finite-differenced using highly conservative schemes (Arakawa and Lamb 1977, 1981). Fourier filtering of the mass flux and pressure gradient vectors is used to maintain computational stability near the poles (Arakawa and Lamb 1977).

A key feature of the GCM is its formulation in terms of a modified sigma coordinate, in which the planetary boundary-layer (PBL) top is a coordinate surface, and the PBL itself is identified with the lowest model layer (Suarez et al. 1983). The mass sources and sinks for the PBL consist of large-scale convergence or divergence, turbulent entrainment, and the cumulus mass flux. Turbulent entrainment can be driven by positive buoyancy fluxes or by shear of the mean wind in the surface layer or at the PBL top.

The cumulus mass flux and the warming and drying of the free atmosphere due to cumulus convection are determined through the cumulus parameterization of Arakawa and Schubert (1974; see also Lord et al. 1982), as modified by Randall and Pan (1993). Quasi equilibrium of the cloud work function is closely approximated through the use of a prognostic cumulus kinetic energy. The ice phase is taken into account in the cumulus parameterization, although it is not included in the large-scale saturation parameterization (but see Fowler et al. 1995). Rain falling through unsaturated grid boxes is allowed to evaporate if it originates through large-scale saturation at an upper level, but not if it originates in cumulus towers. Cumulus friction is taken into account, assuming momentum conservation in the convective updrafts. The effects of convective downdrafts are not currently included.

The Arakawa-Schubert parameterization currently applies only to clouds that draw their mass from the PBL. There are, of course, moist convective motions that originate above the PBL. These are parameterized through a conventional moist convective adjustment, although work is currently under way to remedy this through generalization of the Arakawa-Schubert parameterization to allow clouds to originate at any level.

The radiation parameterization of the model is that of Harshvardhan et al. (1987). The terrestrial radiation parameterization includes cooling due to water vapor,

TABLE 1. List of the discrete biomes defined for use with SiB2.

Biome number	Biome name
1	Broadleaf evergreen trees
2	Tall vegetation: Broadleaf deciduous trees
3	Tall vegetation: Broadleaf and needleleaf trees
4	Tall vegetation: Needleleaf-evergreen trees
5	Tall vegetation: Needleleaf-deciduous trees
6	Short vegetation/C4 grassland
7	Short vegetation: Broadleaf shrubs with bare soil
8	Short vegetation: Dwarf trees/shrubs
9	Agriculture/C3 grassland

carbon dioxide, and ozone. The solar radiation parameterization includes Rayleigh scattering and absorption by water vapor and ozone and simulates both the diurnal and seasonal cycles. A complete (solar and terrestrial) radiation calculation is done once per simulated hour in order to resolve adequately the diurnal cycle and the effects of transient cloudiness. A zonally uniform ozone distribution is prescribed as a function of latitude and height.

Cloudiness can occur in any GCM layer and can be associated with large-scale saturation, PBL stratocumulus clouds, or the anvils of deep cumuli. For simplicity, when and where largescale saturation cloudiness occurs, it is assumed to fill an entire grid box; no parameterization of subgrid fractional cloudiness is attempted. Anvil cloud amount is assumed to be proportional to the cumulus mass flux and is prescribed to be independent of height from 500 mb to the highest level reached by the convection. The constant of proportionality is chosen to make the global albedo 0.3. The optical properties assigned to the clouds are described by Harshvardhan et al. (1989).

Stratocumulus clouds are assumed to be present in the PBL whenever the temperature and mixing ratio at the PBL top (as determined by a mixed-layer assumption) correspond to supersaturation, provided that cloud-top entrainment stability does not occur. The presence of the stratocumulus clouds is felt through both the radiation and entrainment parameterizations. The latter takes into account the generation of turbulence kinetic energy through increased buoyancy fluxes associated with phase changes and highly concentrated cloud-top radiative cooling (Randall 1980, 1984). As a result of these cloud-enhanced buoyancy fluxes, the presence of a stratocumulus layer in the PBL tends to favor more rapid entrainment and, therefore, a deeper PBL. A very simple parameterization of cloud-top entrainment stability is included.

It is important to note that the cloud microphysics parameterization developed by Fowler et al. (1995) because the CSU GCM has not been used in the runs described here. The reason is that SiB2 and the microphysics parameterization have been under development

TABLE 2. Time-independent biome parameters, their units, and their range (if limited).

Time-independent biome parameters	Units	Range
leaf-angle distribution		-1 for vertical, 0 for spherical, 1 for horizontal
local slope angle		0-1
leaf reflectance		0-1
leaf transmission		0-1
stomatal resistance parameters		
optimum temperature for photosynthesis	K	
lowest temperature for photosynthesis	K	
vapor pressure deficit reduction term for photosynthesis		
critical leaf-water potential 1	m	
critical leaf-water potential 2	m	
xylene resistance		
root depth	m	
upper temperature for photosynthesis	K	
maximum root length	m <sup>-3</sup>	
root resistance		
root cross sectional area	m <sup>2</sup>	
soil surface reflectance		0-1
soil moisture potential at saturation	m	
soil porosity		0-1
depth of the soil layers	m	
soil hydraulic conductivity at saturation	m s <sup>-1</sup>	
soil hydraulic parameters		

simultaneously and in parallel and were tested at approximately the same time. We chose to test them separately, of course. We fully intend to use them together in the future.

The versions of the GCM used in this study do not include a gravity-wave drag parameterization, although one is being tested as this is written.

The prescribed boundary conditions of the GCM include realistic topography and the observed climatological seasonally varying global distributions of sea surface temperature and sea ice thickness. The surface albedo of the ocean is zenith-angle dependent. We also

TABLE 3. Seasonally varying biome parameters, their units, and their range of values (if limited).

Seasonally varying biome parameters	Units	Range
leaf-area index		
leaf greenness		0-1
canopy height	m	
canopy base	m	
vegetation cover fraction		0-1
surface roughness	m	
zero plane displacement	m	
leaf bulk boundary-layer resistance coefficient	(m s <sup>-1</sup> ) <sup>-1/2</sup>	
canopy resistance coefficient		
root length		

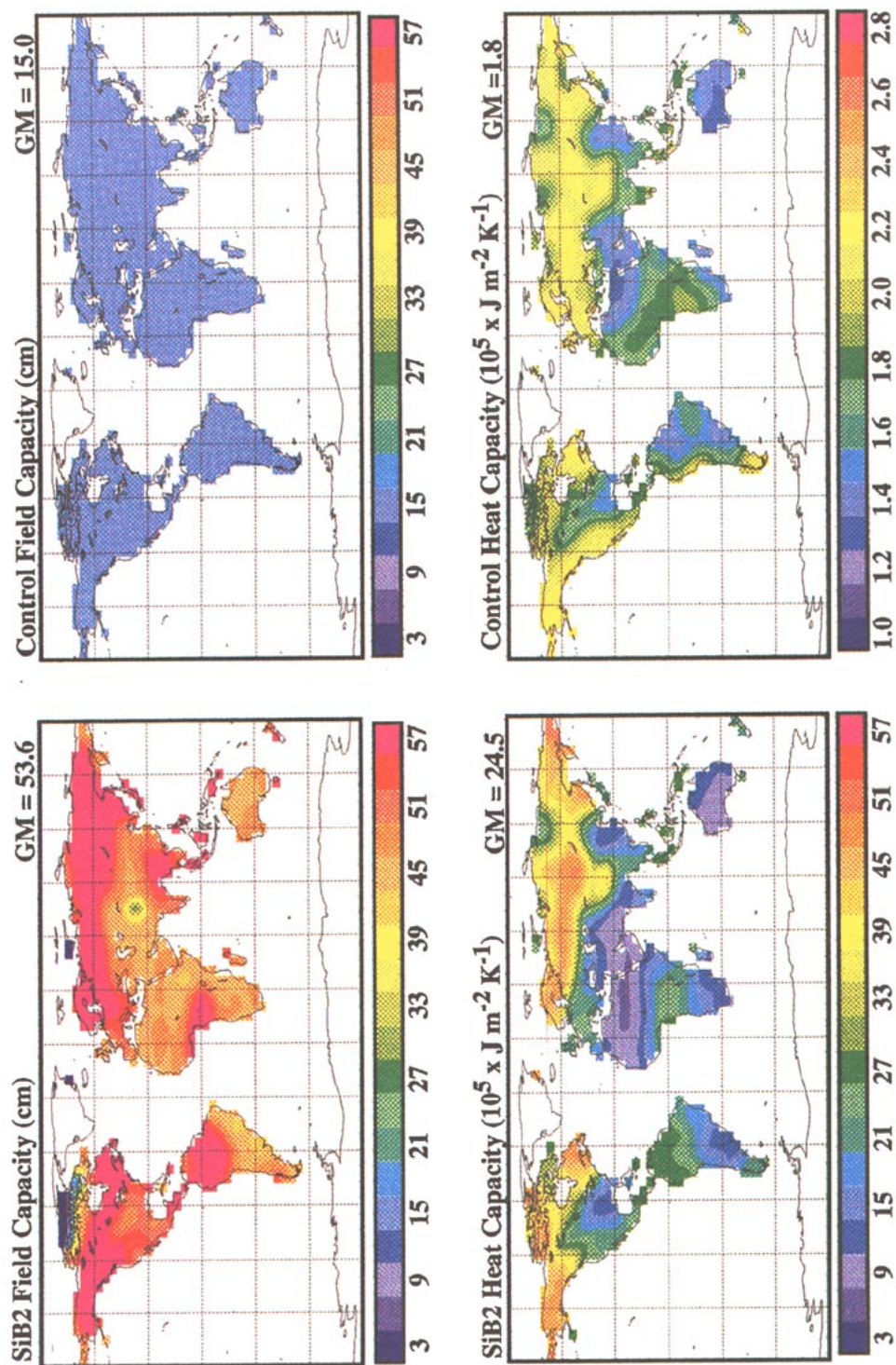


FIG. 1. (a) Field capacity associated with top two soil layers as used by SiB2. (b) Field capacity of the bucket model in the control run. (c) Soil heat capacity in the SiB2 run. (d) Soil heat capacity in the control run.

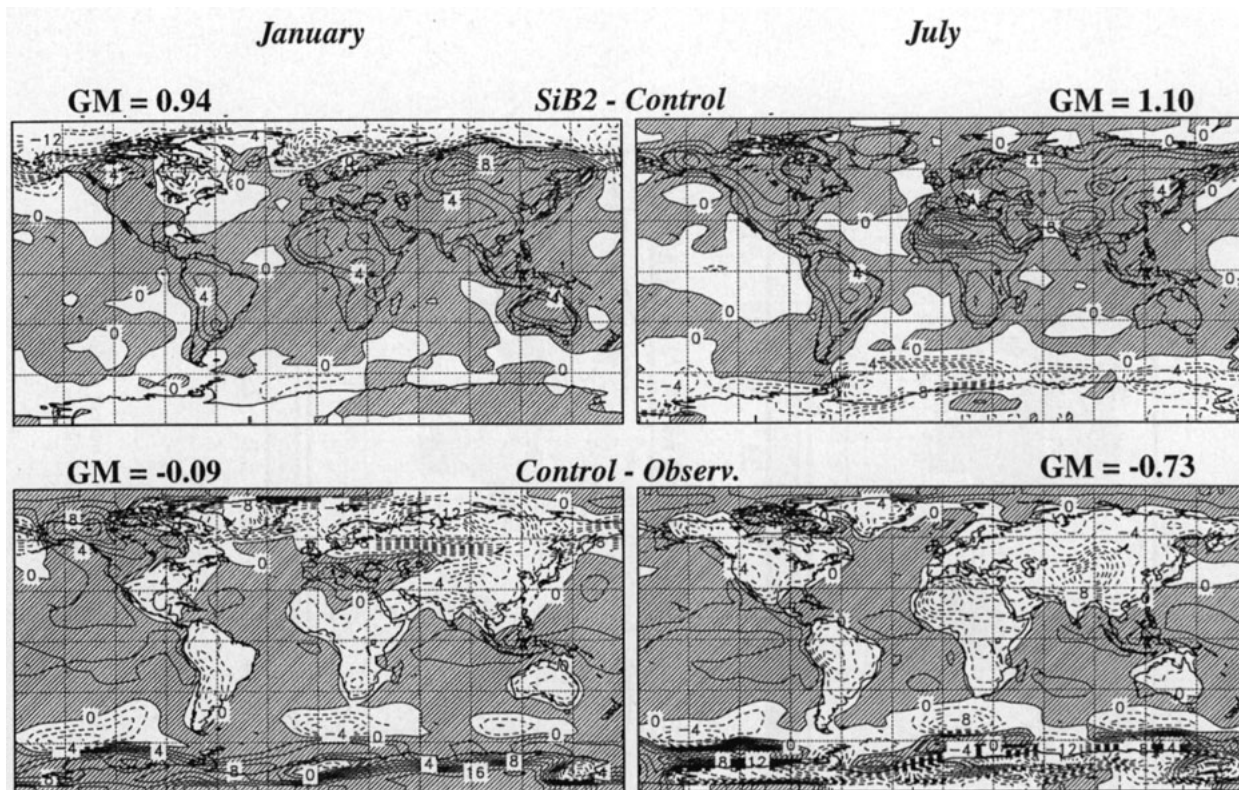


FIG. 2. Maps of surface air temperature differences between SiB2 and the control and between the control and the observations of Legates and Willmott (1990a) for January and July. Positive values are hatched. The contour interval is 2 K.

prescribe the soil characteristics and the seasonally varying morphological and physiological parameters for the land-surface vegetation, as described in the section 2d.

#### b. SiB2

The formulation of SiB2 is described in detail in Part I. In brief, it is based on a single vegetation canopy layer overlying a three-layer soil model. It makes use of a biophysically realistic description of stomatal resistance that is directly coupled to a photosynthesis model. Precipitation can be intercepted by the canopy before reaching the soil. A parameterization of patchy snow is also included. As an interesting diagnostic with important future applications, the model determines the rate at which carbon is incorporated into the vegetation through photosynthesis, that is, the gross primary productivity (GPP).

The introduction of SiB2 has led to many changes in the GCM, relative to the “control” version of the model. A summary of these differences is as follows.

(i) SiB2 introduces a deep soil temperature as well as a surface soil temperature. The control model has a single soil temperature. The heat capacity associated with the deep soil temperature is large enough to represent

the storage of heat on annual timescales. The heat capacity associated with the surface soil temperature is appropriate to represent the diurnal cycle. This idea can be traced to the work of Deardorff (1977).

(ii) SiB2 introduces three ground wetnesses, representing water that is below the surface of the soil.

(iii) SiB2 introduces two surface moisture stores, representing moisture that is sitting on top of the soil (as in puddles after a precipitation event) and on the canopy (as in leaves wetted by rain or dew), respectively. The control model has only one ground wetness and no surface stores other than snow.

(iv) The moisture storage capacity of the soil in the control run is 15 cm everywhere, while in the SiB2 run it varies geographically and is generally much larger than 15 cm.

(v) SiB2 introduces a stomatal resistance that limits the evapotranspiration, that is, restricts the flow of moisture from the soil to the atmosphere. The control version of the model uses a “bucket” hydrology with a simple exponential dependence of soil moisture availability on the amount of soil moisture present relative to field capacity. As discussed in Part I, the stomatal resistance is prognosed, mainly for computational convenience.

(vi) SiB2 introduces a “patchy snow” parameterization that allows the surface albedo to gradually



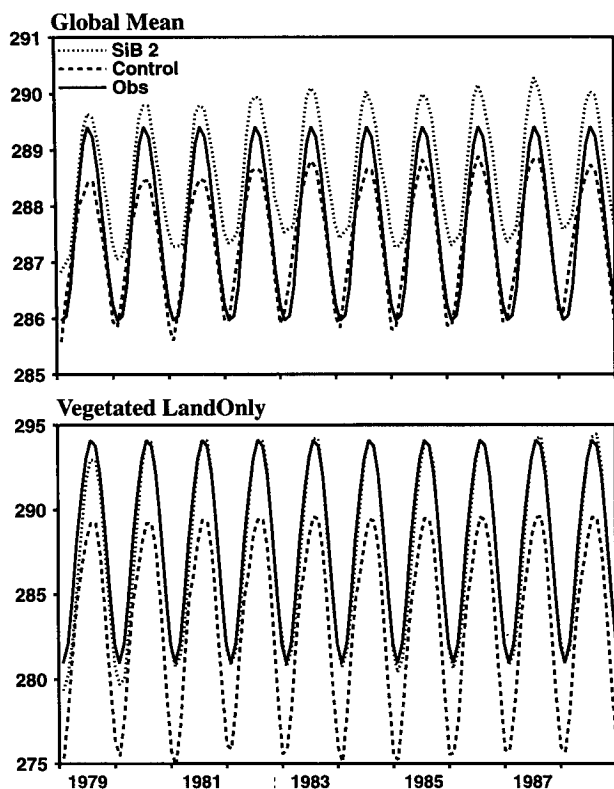


FIG. 3. Time series of the globally averaged land surface temperature (i.e., ocean surface temperatures are not included). The results are based on monthly means for all 120 months of both the SiB2 run and the control.

change from that of bare ground to that of snow as the snow depth increases. The control version of the model assumes uniform snow cover whenever snow is present, no matter how small the amount.

#### c. Coupling of SiB2 with the GCM

The time-differencing scheme of the GCM is quite complicated because of the many diverse processes that

must be represented. In broad terms, the “dynamics” is integrated with a relatively short time step, nominally 7.5 minutes for the “medium-resolution” model discussed later, while the “physics” is integrated with a longer time step, nominally one hour for all versions of the model. The surface fluxes are computed with a partially implicit scheme similar to that described by Sato et al. (1989a); until recently, the longer physics time step was used for this purpose. During the implementation of SiB2 in the GCM, however, we decided to implement the surface fluxes on the shorter dynamics time step. There are two reasons: first, the strong diurnal cycle of the surface fluxes over land argues against a 1-h time step from the point of view of numerical accuracy; second, the strong dependence of the surface transfer coefficients on the near-surface static stability introduces a strong nonlinearity into the surface flux parameterization that can cause wild oscillations if a longer time step is used (e.g., Kalnay and Kanamitsu 1986). Not surprisingly, the numerical solution is considerably better behaved with the shorter time step.

The numerical methods outlined above were introduced in the process of incorporating SiB2 into the GCM, but the same methods were used in both the SiB runs and the control runs described later in this paper.

#### d. Land-surface boundary condition datasets

Table 1 lists the nine discrete biomes defined in SiB2. Part II gives a map showing the prescribed geographical distribution of biomes. The data were originally compiled at a resolution of 1° of latitude by 1° of longitude. They were subsequently averaged onto coarser grids for use in the model. The runs discussed in this paper used a horizontal grid with cells 4° of latitude by 5° of longitude. Numerous parameters are associated with each biome and are geographically distributed according to the distribution of biomes via look-up tables (see Part II). The time-independent biome parameters are listed in Table 2, while the seasonally varying biome parameters are listed in Table 3.

TABLE 4. A list of the SiB2 soil types and associated parameters.

Soil type	Soil moisture potential factor	Soil potential at saturation (m)	Hydraulic conductivity at saturation ( $\text{m s}^{-1}$ )	Soil Porosity	Cosine of mean slope	Description
1	4.05	-0.04	$1.76 \times 10^{-4}$	0.40	0.1736	sand
2	4.90	-0.07	$3.5 \times 10^{-5}$	0.44	0.1736	sandy loam
3	5.39	-0.15	$7.0 \times 10^{-6}$	0.45	0.1736	loam
4	7.12	-0.12	$6.3 \times 10^{-6}$	0.42	0.1736	clay loam
5	8.52	-0.36	$2.5 \times 10^{-6}$	0.48	0.1736	clay
6	4.05	-0.04	$1.76 \times 10^{-4}$	0.40	0.1736	ice (assigned sand)
7	5.39	-0.15	$7.0 \times 10^{-6}$	0.45	0.1736	organic (assigned loam)

TABLE 5. Ten-year averages of the differences between the SiB2 run and the control.

Field	(a) January			(b) July		
	Land	Ocean	Global	Land	Ocean	Global
Precipitation ( $\text{mm day}^{-1}$ )	-0.3419	-0.2687	-0.2905	-0.9769	-0.2687	-0.4677
Evaporation ( $\text{mm day}^{-1}$ )	-0.8620	-0.0491	-0.2938	-1.3241	-0.0944	-0.4646
$P - E$ ( $\text{mm day}^{-1}$ )	0.5209	-0.2195	0.0033	0.3471	-0.1539	-0.0031
Precipitable water (mm)	-0.9075	-0.5025	-0.6248	-0.8220	-0.1365	-0.3429
Net surface shortwave radiation (SW) ( $\text{W m}^{-2}$ )	9.7480	1.74132	4.1517	24.3918	1.0282	8.0620
Net surface LW ( $\text{W m}^{-2}$ )	18.7572	1.4270	6.6444	26.2324	0.3949	8.1734
Sensible heat flux ( $\text{W m}^{-2}$ )	23.1548	-1.4935	5.9269	38.9356	-1.1036	10.9504
Latent heat flux ( $\text{W m}^{-2}$ )	-25.1426	-1.4342	-8.5718	-38.6208	-2.7559	-13.5533
Net surface energy flux ( $\text{W m}^{-2}$ )	-7.0214	3.2421	0.1522	-2.1552	4.4929	2.4914
Clear-sky net surface SW ( $\text{W m}^{-2}$ )	-0.3279	-0.8600	-0.6998	1.0243	-1.1426	-0.4902
Surface albedo (%)	-1.3143	0.4256	-0.0995	-0.6924	0.7137	0.4672
Clear-sky sfc albedo (%)	-0.8760	0.4151	0.0253	-0.1416	0.4151	0.0253
Total cloudiness (%)	-4.4467	-0.8479	-1.9314	-6.7676	-0.3902	-2.3102
PBL depth (mb)	12.3161	-2.9490	1.6458	11.2141	-2.9490	0.6225
Maximum PBL depth (mb)	14.5692	-1.6422	3.2383	13.9028	-5.4090	0.4049
PBL wind speed ( $\text{m s}^{-1}$ )	0.4043	-0.0900	0.0587	0.4276	0.0509	0.1643
Turbulence kinetic energy ( $\text{m}^2 \text{s}^{-2} \times 10^{-2}$ )	3.5472	-0.5850	0.6590	5.4708	-0.0781	1.5924
PBL mixing ratio ( $\text{g kg}^{-1}$ )	-0.8781	0.0076	-0.2590	-1.2216	0.1180	-0.2852
Surface mixing ratio ( $\text{g kg}^{-1}$ )	-0.8757	0.0075	-0.2583	-1.2174	0.1174	-0.2844
PBL potential temperature (K)	4.7064	0.0383	1.4436	4.2853	0.0580	1.3307
Surface air temperature (K)	4.5085	0.0867	1.4179	4.0731	0.0991	1.2955
Ground temperature (K)	4.8118	-0.0031	1.4464	4.1780	-0.0063	1.2622
Snow on ground (mm)	-15.2451	n/a	-4.5896	-16.0754	n/a	-4.8396
Soil moisture (gw1, gw2 only) (mm)	-46.0534	n/a	-46.0534	-9.4324	n/a	-9.4324

The soil types, soil reflectances, and seasonally varying Normalized Difference Vegetation index (NDVI) are also prescribed from observations using methods discussed in Part II. These maps are given in Part II and will not be repeated here. Table 4 lists the parameters associated with each soil type and gives their assigned values. From the NDVI and the biome we determine the fraction of photosynthetically active radiation absorbed by the green canopy, or FPAR, by methods explained in Part II. Maps of the global distribution of the FPAR are also shown in Part II. The seasonal change in FPAR over the Northern Hemisphere continents is quite spectacular.

Figure 1 shows the field capacity, that is, the capacity of the soil to hold moisture, for the top two soil layers only with SiB2 and for the single-layer "bucket" used in the control run described later. With SiB2, the upper two are those whose moisture is directly available for surface evaporation. An important point is that the field capacity prescribed for use with SiB2, which is based on root depths and soil porosities, is much larger than the uniform 15 cm used with the bucket model. Using a version of the GFDL (Geophysical Fluid Dynamics Laboratory) GCM with a bucket model, Milly and Dunne (1994) showed strong sensitivity of the global hydrologic cycle to the water-holding capacity of the land, such that increased holding capacity led to more evaporation from the continents and less runoff.

Also shown in Fig. 1 is the heat capacity of the soil. For the control run described later, this is the heat capacity of the single soil layer considered. For SiB2, it is the heat capacity of the deeper soil layer (see Part I). The heat capacity of the upper soil layer in SiB2 is roughly the same as the total soil heat capacity in the control. In both versions of the model, the capacity of the soil depends on the soil moisture content. To make the plots shown in Fig. 1, we have used annual mean soil moistures from the control run and the SiB2 run presented later. Note that the heat capacity of the soil is much larger in the SiB2 run than in the control; the color scales used in the two maps are different. This has important consequences for winter temperatures, as will be discussed later.

The surface roughness datasets used are shown in Part II. This roughness is associated with vegetation only; orographic roughness is not included since it can be incorporated through a gravity wave drag parameterization. The seasonal change of the vegetative roughness of the Northern Hemisphere continents is quite noticeable.

To compute the surface albedo, we use the soil reflectance, the leaf-area index, and the biome type, as explained in Part II.

The surface albedo and surface roughness datasets used in the SiB2 simulations described in this paper are the same as those used in the control, that is, exactly

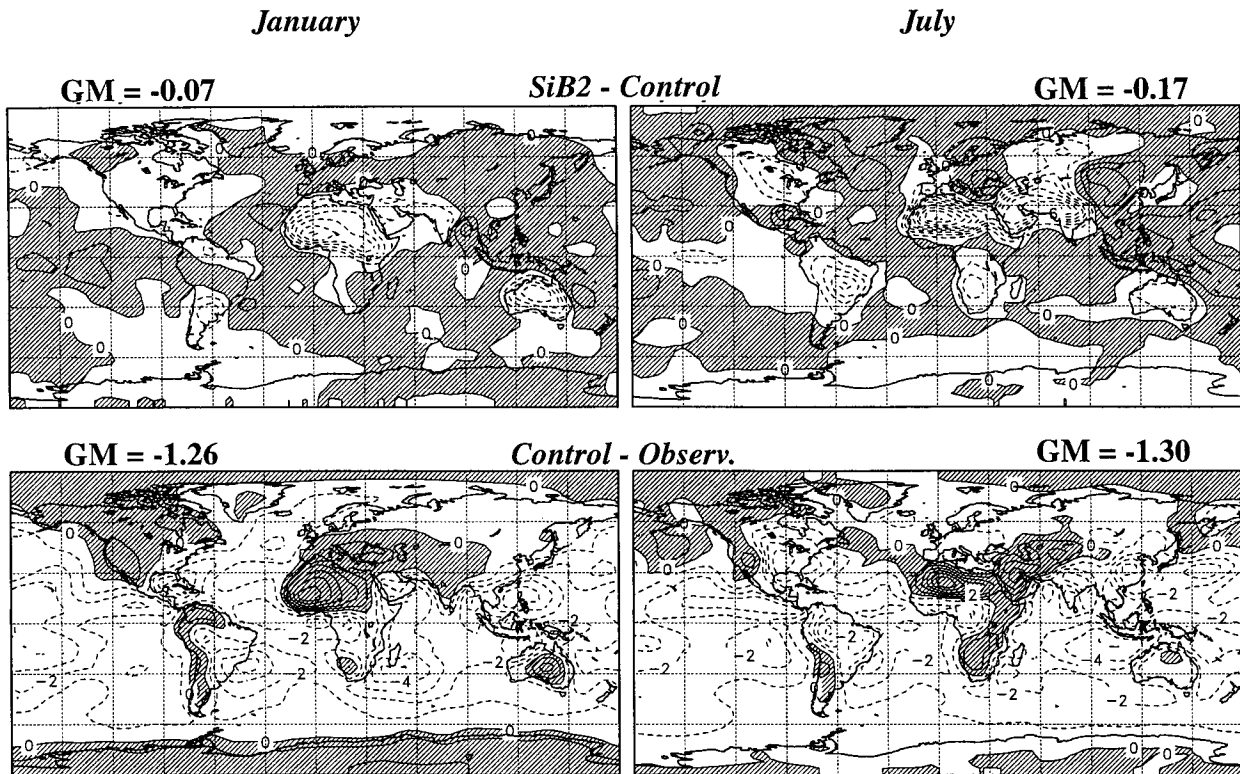


FIG. 4. Maps of surface air mixing ratio differences between SiB2 and the control and between the control and the ECMWF observations for January and July. Positive values are hatched. The contour interval is  $1 \text{ g kg}^{-1}$ .

the same methods are used to determine these quantities in both runs. This means that the differences between the two runs are due to the different physical parameterizations used and not due to differences in the input data.

### 3. A brief discussion of the problems encountered with SiB1

As discussed above, results obtained with SiB1 in the UCLA/GLA model were never published because of problems that were encountered. Specifically, when run with SiB1 the hydrological cycle of the simulated land surface essentially ground to a halt. The ground dried out over a period of a simulated year or two, and the simulated continental evaporation and precipitation rates decreased to values much less than those observed. This catastrophe did not occur when the same GCM was run with a more conventional "bucket model" hydrology.

The cause of the problem was determined to be excessive stomatal closure in response to environmental stresses. We have accordingly named the phenomenon "stomatal suicide." Although our experiences with stomatal suicide in the GCM were neither realistic nor pleasant, we believe that the problem we encountered represents an exaggeration of a real phenomenon that

needs to be understood and appreciated. One goal in the design of SiB2 was the elimination of stomatal suicide. We succeeded in achieving this goal.

When the PBL is warm and dry, the vegetation responds by increasing its stomatal resistance, thus limiting the rate of evapotranspiration. This is an adaptation that allows the plants to conserve scarce moisture. As the evapotranspiration decreases, the PBL tends to become warmer and drier, thus favoring a further increase in stomatal resistance and a further decrease in evapotranspiration. This is a positive feedback loop. If the stomatal resistance is permitted to increase to infinity, essentially cutting off all evapotranspiration, the surface temperatures can increase and the ambient moisture can decrease to the point that the vegetation would be killed over a period of time. In this unrealistic limit, the "adaptive response" of shutting down evapotranspiration inadvertently leads to death. In reality, of course, there is an upper limit to the stomatal resistance and a corresponding lower limit to the evapotranspiration, such that the plants can survive episodes of warm, dry weather. This phenomenon seems to have been particularly evident in the UCLA/GLA GCM implementation, probably because of the direct contact permitted between the canopy and the atmospheric conditions within a deep, well-mixed boundary-layer



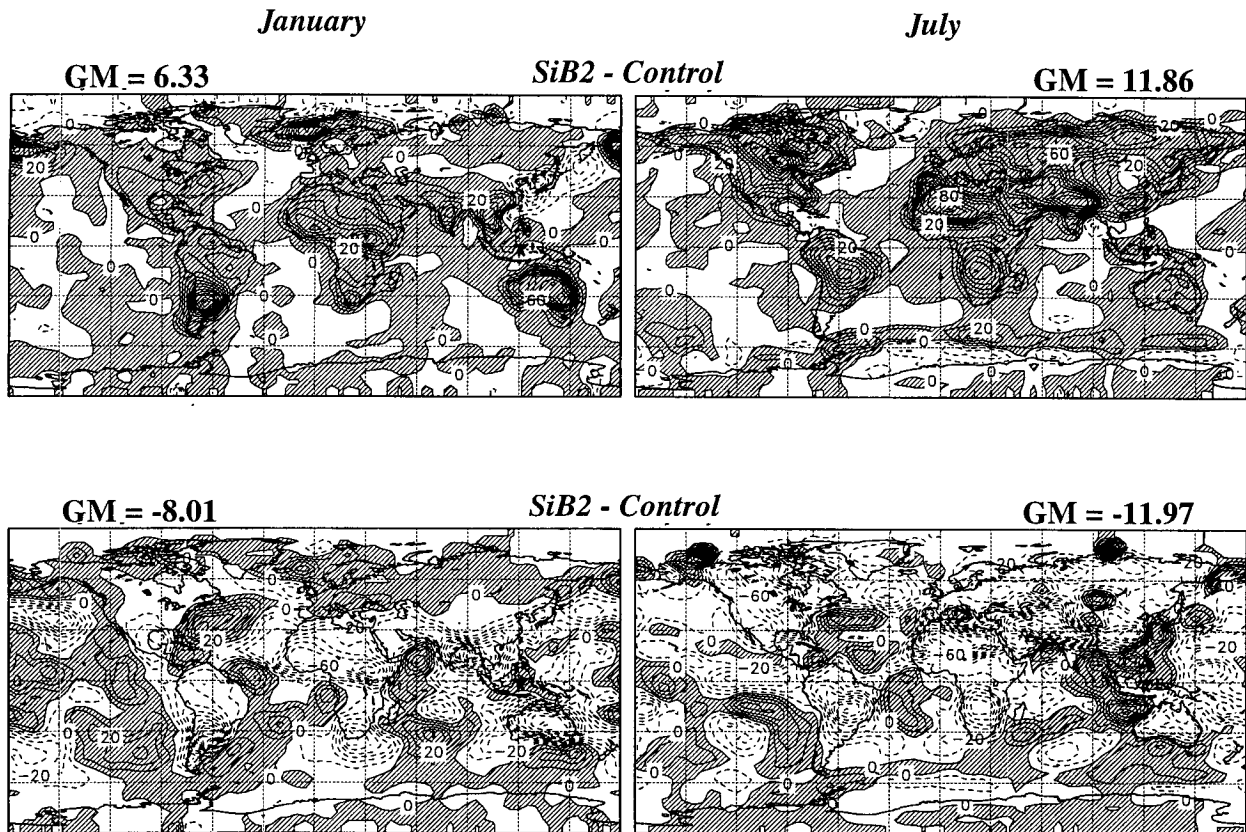


FIG. 5. Maps of surface sensible heat flux (top two panels) and latent heat flux (bottom two panels) differences between SiB2 and the control, January and July. The contour interval is  $10 \text{ W m}^{-2}$ .

model. In the implementation described by Sato et al. (1989a), the PBL was represented by up to six of the lowest layers of the atmospheric model; these layers were usually not well mixed. As a result, the stomatal suicide effects, while occasionally observed in the Sato et al. (1989a) implementation, were never very harsh. As discussed in Part I, SiB2 includes a more realistic parameterization of stomatal closure in response to temperature and moisture stress.

#### 4. Results and comparison with a control run and with observations

##### a. Experiment design

Two 10-yr simulations were made with a grid spacing of  $4^\circ$  of latitude by  $5^\circ$  of longitude with 17 layers. These simulations were identical except that one used SiB2 to represent the biophysics of the land surface (the “experiment”), while the other used a “bucket hydrology” model (the “control”). In particular, as mentioned earlier, the control run used the same surface albedo and surface roughness datasets as the experiment.

The atmospheric variables of the SiB2 run were initialized using a 1 October restart from a previous model

run without SiB2. For SiB2 run, the canopy water storage was initialized everywhere to zero, and the stomatal conductance was initialized to  $0.01 \text{ s m}^{-1}$ . The two ground temperatures were both set equal to the single ground temperature obtained in an earlier run of the model without SiB2.

The three soil moisture components were initialized from the soil moisture data (Y. Mintz 1983, personal communication) using a procedure incorporating SiB2 and NDVI data as follows. The SiB2 biome-dependent parameters soil depth, soil porosity, soil moisture potential factor, soil potential at saturation, leaf potential, and vegetation cover fraction were used to transform the one-layer Mintz and Serafini soil wetness fraction into an equivalent SiB2 soil moisture value using a procedure outline by Sato et al. (1989b, appendix D). The basis for the method is simple. A grid square is assumed to be saturated at time  $t = 0$ , and thereafter exposed to an evaporative demand. A look-up table of drying times and soil moisture contents is then generated, which allows us to translate the Mintz–Serafini values into SiB2 values on the basis of equal drying times. For simplicity, we assumed that the initial soil moisture concentration was vertically uniform. The initial frac-

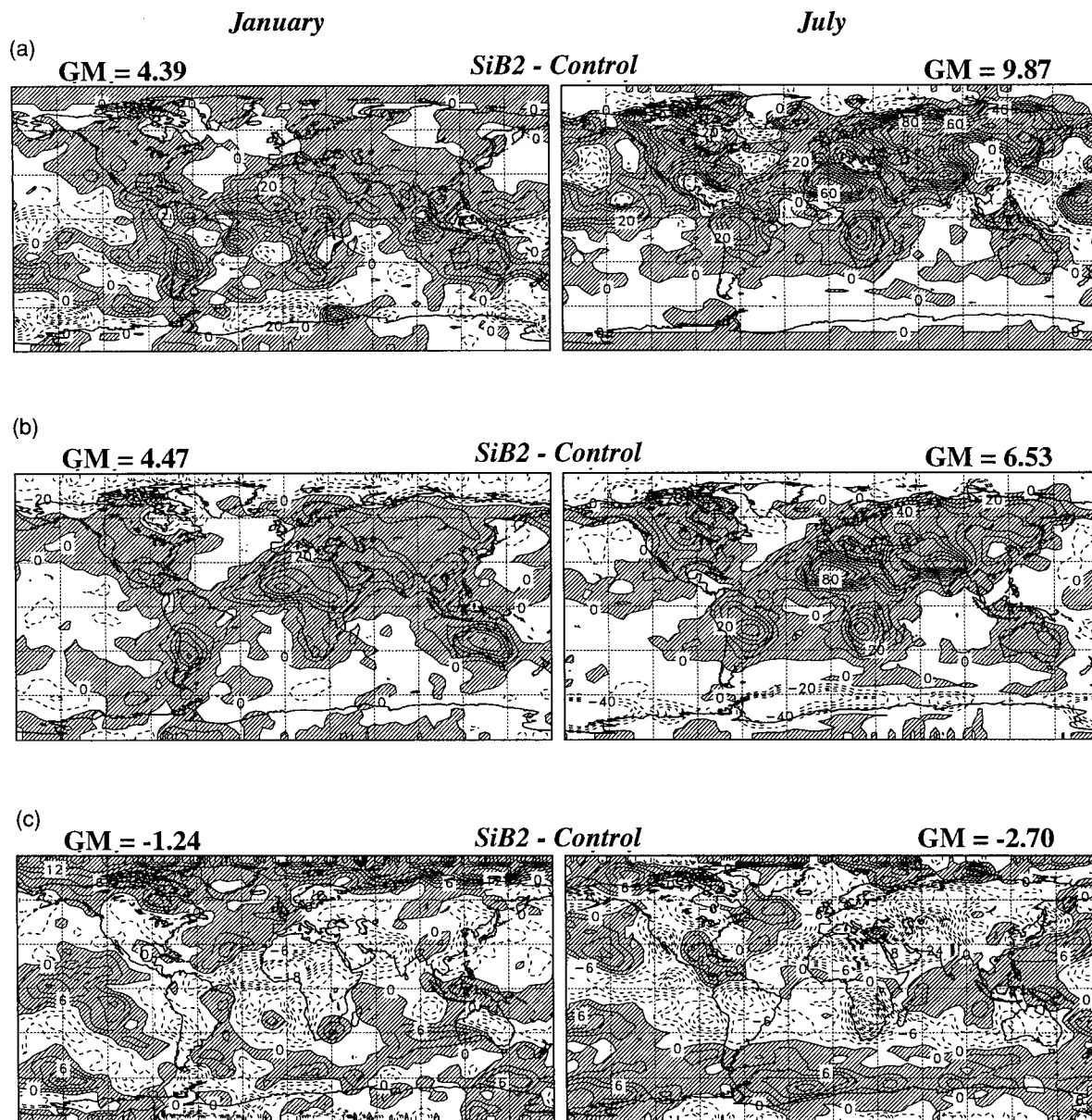


FIG. 6. Maps of January and July differences between SiB2 and the control for (a) solar radiation absorbed by the surface; (b) net surface longwave radiation; and (c) total cloudiness. The contour interval is  $10 \text{ W m}^{-2}$  for the radiation fluxes and 3% for the cloudiness.

tion of photosynthetically active radiation (FPAR) value for the grid square was used to impose a lower limit on the initial soil moisture where the presence of vegetation, as observed by satellite, indicates that there is more soil moisture than the Mintz–Serafini data would suggest. This limit takes the form  $W > 0.5 \times \text{FPAR} + 0.1$ .

The test of SiB2 was run from 1 October to 15 December using climatological sea surface temperatures (SSTs) and ice cover, and from 15 December to 15 January using SSTs linearly interpolated between the

December climatology and January 1979 data. The run continued for ten years through December 1988 using real SST and ice cover data. Here climatology is defined as the 1979 through 1988 10-yr mean. The SST and ice-cover boundary conditions were created from a  $2.5 \times 2.5$  degree resolution dataset for 1979–1988, as compiled for the Atmospheric Model Intercomparison Project (AMIP; Gates 1992).

The control run was initialized using a restart record from 1 December of the experiment. The soil moisture was initialized from a 1 December restart from the end

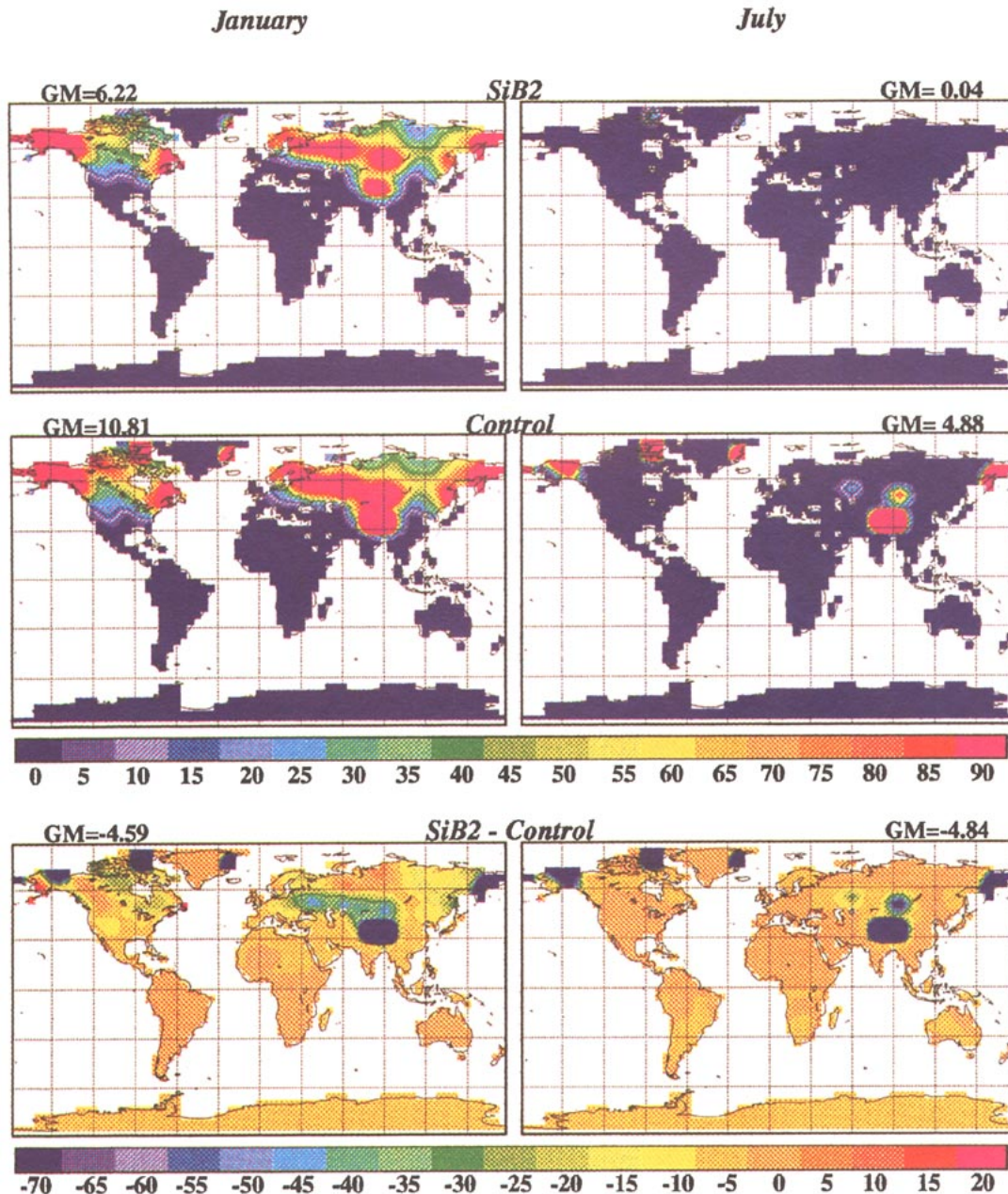


FIG. 7. Maps of the snow mass, expressed as millimeters of liquid water equivalent on the ground (or equivalently as  $\text{kg m}^{-2}$ ), for experiment, control, and difference for January and July.

of a prior 10-yr simulation without SiB2, so as to be reasonably well adjusted.

#### *b. The effects of SiB2 on the simulated climate*

Figure 2 shows maps of surface air temperature differences between SiB2 and the control and between the control and the observations of Legates and Willmott (1990a) for January and July. For both model runs, we used the temperature corresponding

to the potential temperature of the mixed layer evaluated at the surface pressure. Since potential temperature tends to increase upward in the boundary layer, this method may tend to give overestimates of the surface air temperature. The simulated averages were computed by sampling every hour so that the diurnal cycle is very well resolved. A more revealing comparison might involve daily maximum and minimum temperatures, but unfortunately the necessary data was not saved in the simulations.

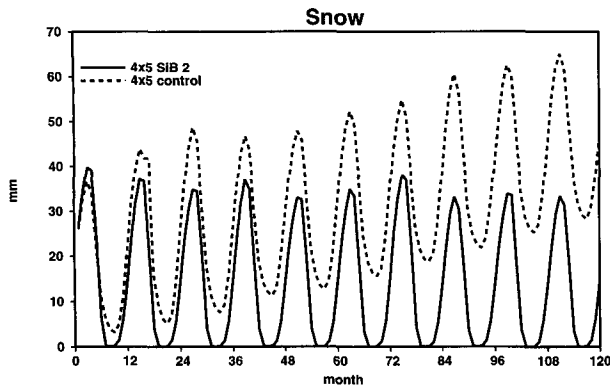


FIG. 8. Time series of the globally averaged snow mass for the SiB2 run and the control (units are mm of water, which is equivalent to  $\text{kg m}^{-2}$ ).

The control is generally colder than observed over the continents. SiB2 leads to a general and fairly dramatic warming of the surface air temperature over the continents relative to the control. The ground temperature and PBL potential temperature undergo similar increases (not shown). In fact, the map of the differences in surface air temperature between the SiB2 run and the control run looks quite similar to the map of the errors in the control run relative to the observations. In many parts of the world, the warming in the SiB2 run results from the increased sensible heat flux and the decreased latent heat flux; those fields are discussed below in connection with Fig. 5. An example is the Sahara. The bucket model of the control run makes the evapotranspiration equal to a prescribed monotonically increasing function of soil wetness as a fraction of the field capacity multiplied by the potential evapotranspiration. The potential evapotranspiration of course increases exponentially with the ground temperature. In very hot places like the Sahara, the bucket model can predict substantial evapotranspiration even when the

soil is very dry. For this reason, the bucket model tends to overpredict the evapotranspiration in desert regions. SiB2, with its biophysically based parameterization of evapotranspiration, does not suffer from this problem, and so it produces much weaker and more realistic evapotranspiration rates over the deserts.

Figure 3 shows a time series of the simulated land surface temperature for both runs. The SiB2 run shows a slow warming trend of about one degree over the ten simulated years. Table 5 gives global means of the surface air temperature and many other quantities for land, ocean, and total, for both the experiment and control.

Figure 4 shows maps of surface air mixing ratio differences between SiB2 and the control and between the control and the 1987 ECMWF analyses for January and July. The SiB2 run is considerably drier than the control over land, particularly over deserts, but also in other regions such as central North America and the Amazon basin in July. The mixed-layer mixing ratio would normally be somewhat smaller than the surface air mixing ratio. In many places (e.g., the Sahara) SiB2 corrects the excessive humidity of the control. On the other hand, there are some places in which the control is already too dry (e.g., eastern North America) and SiB2 exacerbates the problem.

Figure 5 shows the simulated surface sensible and latent heat flux differences between the SiB2 run and the control. The surface sensible heat flux increases in the experiment, relative to the control, and the surface latent heat flux correspondingly decreases. These changes in the sensible and latent heat fluxes are perhaps the most obvious and expected effects from the introduction of a parameterization of the biophysics of the land surface. They are consistent with the increase in the surface air temperature and the decrease in the surface mixing ratio if we interpret the change in each flux as causing the change in the corresponding mean-state variable, rather than vice versa. It is interesting and well worth noting that the change in the flux drives the change in the mean state, rather than the reverse.

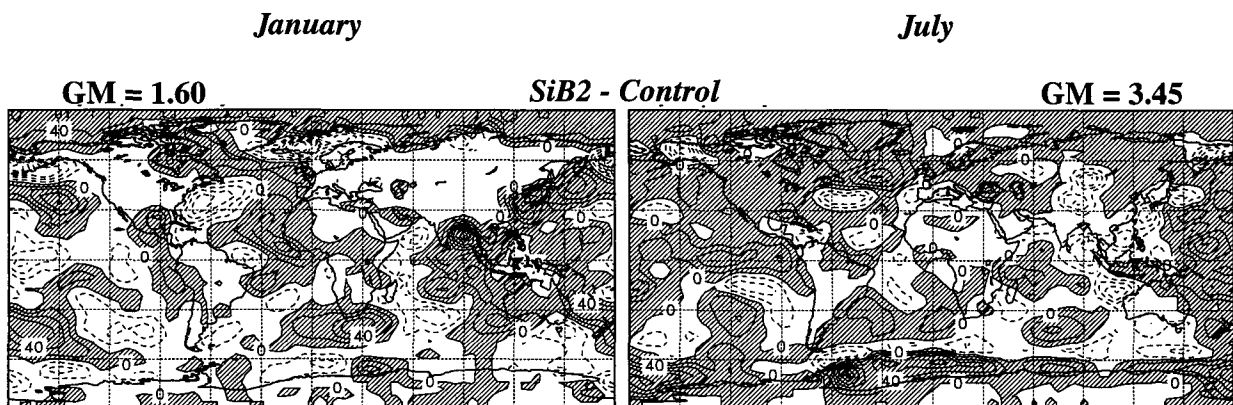


FIG. 9. Maps of net surface energy flux difference between SiB2 and the control for January and July. The contour interval is  $20 \text{ W m}^{-2}$ .



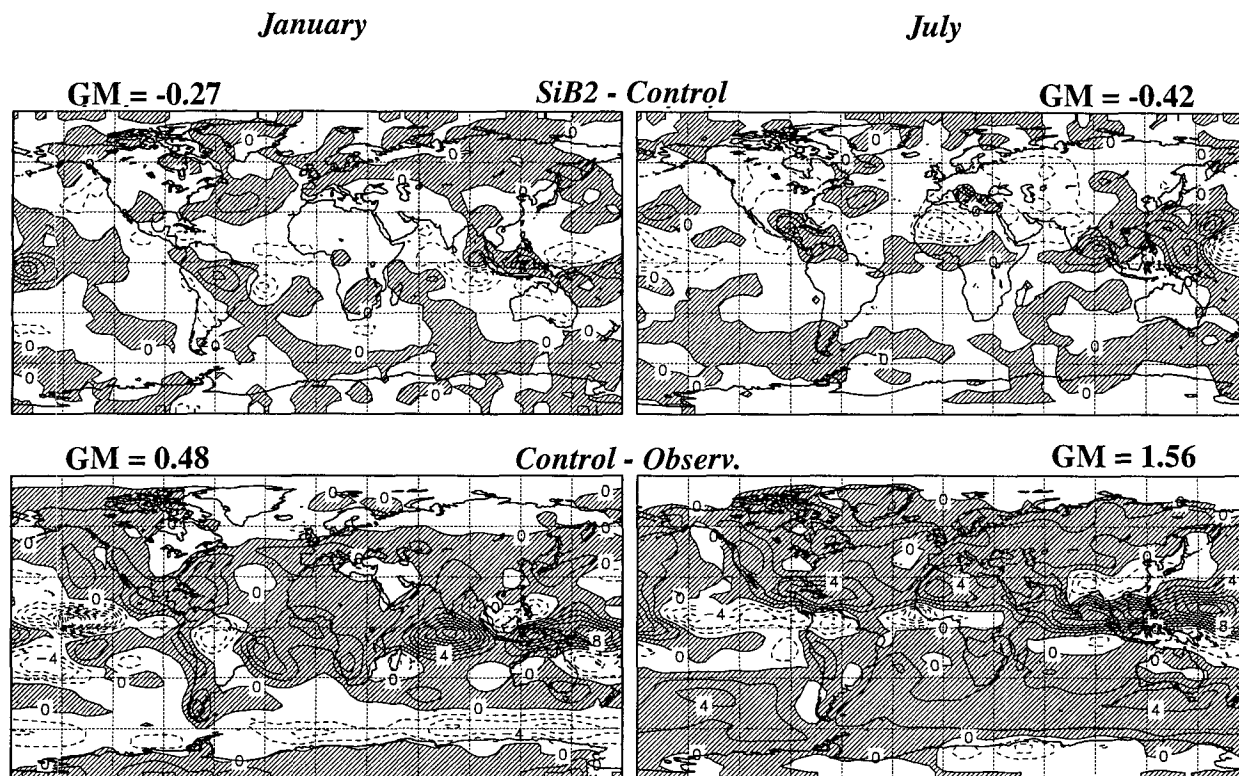


FIG. 10. Maps of the total precipitation rate differences between SiB2 and the control and between the control and the observations of Legates and Willmott (1990b) for January and July. The contour interval is  $2 \text{ mm day}^{-1}$ .

Figure 6 shows the solar radiation absorbed by the surface for experiment, control, and the difference. There is a large increase in absorbed solar radiation in the experiment, relative to the control. The increase is on the order of  $50 \text{ W m}^{-2}$  or more in many places over the continents. The increase occurs in the Tropics throughout the year and over the Northern Hemisphere continents in summer. Comparison of the clear-sky so-

lar radiation absorbed by the surface between the experiment and control (not shown) reveals that the differences seen in Fig. 6 are almost entirely due to cloud effects. Figure 6 also shows that the net surface long-wave radiation (positive upward) has increased substantially virtually everywhere over the continents, indicating that SiB2 leads to more longwave cooling of the surface. The increase is most dramatic over the de-

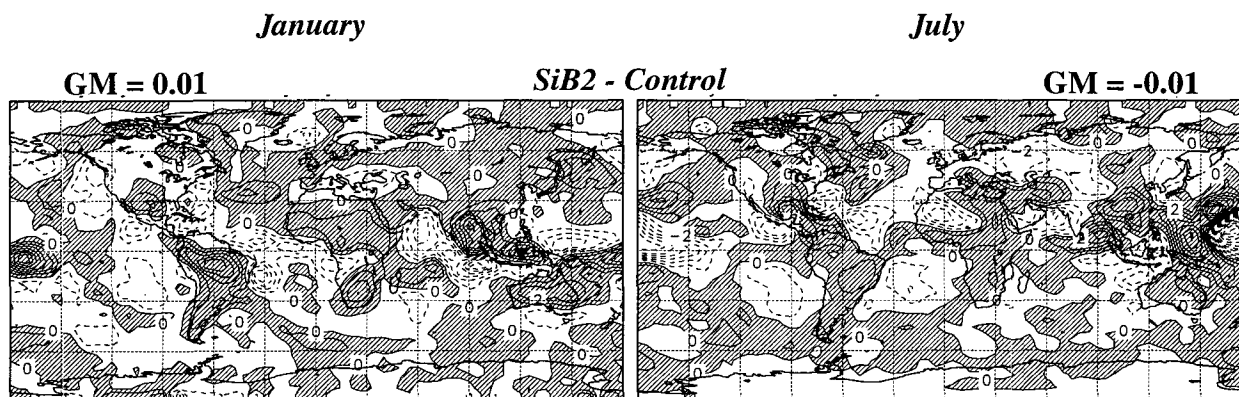


FIG. 11. Maps of the difference in the simulated excess of precipitation over evaporation between SiB2 and the control for January and July. Positive values are hatched. The contour interval is  $1 \text{ mm day}^{-1}$ .



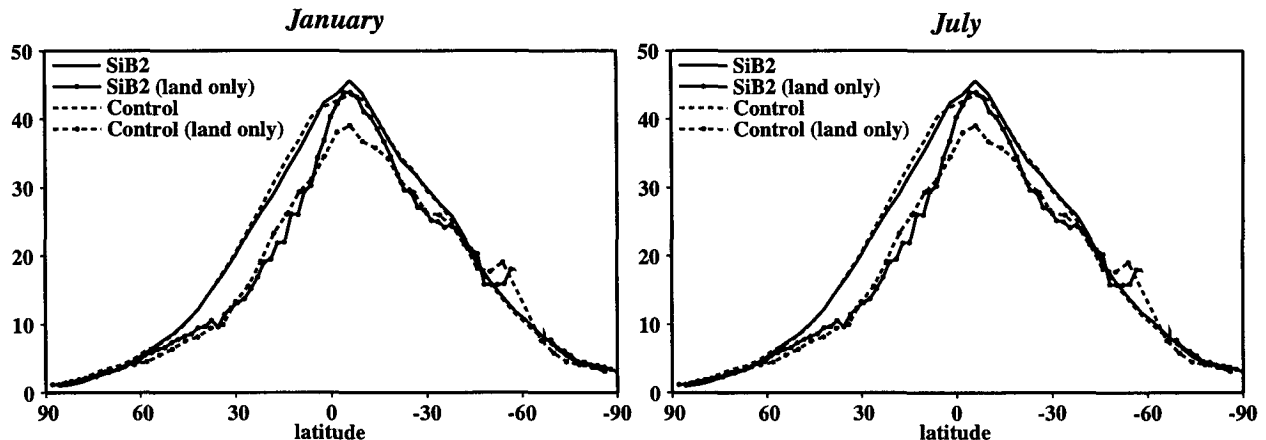


FIG. 12. Zonally averaged precipitable water (the vertically integrated water vapor content) for the SiB2 simulation and the control for January and July. Zonal means for land only are plotted separately.

serts, and it is consistent with the surface warming (more upwelling longwave) and low-level drying (less downwelling longwave) discussed earlier. Finally, Fig. 6 shows that the cloudiness has decreased over most of the continents, both in summer and in winter. This decrease in cloudiness is consistent with the drier, warmer air near the surface, as discussed above. The correlations between the changes in cloudiness and the changes in the surface shortwave and longwave radiation are quite obvious.

Figure 7 shows the maps of the snow mass expressed as millimeters of liquid water equivalent on the ground (or equivalently as  $\text{kg m}^{-2}$ ). SiB2 leads to a general reduction in snow mass in January relative to the control. This is to be expected in view of the "patchy snow" parameterization, included in SiB2 but not in the control. Figure 8 shows a time series of the globally averaged snow mass for both runs (areas of permanent snow and ice in places like Antarctica and Greenland are not included here). In the control run, the snow mass increases relentlessly, although the area covered by snow is not increasing (not shown). SiB2 succeeds in melting almost all snow during the northern summer, and there are no significant trends. We are currently conducting a more detailed analysis of the snow simulations obtained with the model.

The net surface energy flux is defined as the sum of the solar radiation, the longwave radiation, the sensible heat flux, and the latent heat flux, with the signs chosen in such a way that a positive value of the net surface energy flux indicates a net energy flow downward into the atmosphere–soil interface. In both runs, the monthly mean net surface energy flux is very close to zero almost everywhere over the continents, except where snow is melting in July. Figure 9 shows that the flux of energy out of the ocean over the warm waters on the east coast of Asia is greatly reduced in the SiB

run. This is consistent with the warming of the air over Siberia, relative to the control, because it is the flow of cold air off the continents that forces energy up out of the warm western boundary currents in winter. Notice, however, that the flux of energy out of the ocean actually increases over the Gulf Stream. This is due to an increased latent heat flux in that region, as shown in Fig. 5. The reason is discussed later.

As shown in Fig. 10, the precipitation rate generally decreases over land in the SiB2 run relative to the control. This would be expected in view of the decreased evapotranspiration. The precipitation rate shows a tendency to increase in the monsoon regions, however, especially the Amazon basin in January and equatorial Africa and Southeast Asia in July. Figure 10 also shows a comparison of the simulated precipitation of the control run with observations according to Legates and Willmott (1990b). The agreement is generally improved in the experiment, relative to the control, but a glaring problem is the failure of the model to produce a precipitation maximum on the west coast of India in July. This problem occurs both with and without SiB2. The model does produce a Somali jet and some other aspects of the Asian summer monsoon, but the simulated precipitation tends to remain to the south, over the Indian Ocean, rather than moving on shore. We have found that recent changes to the model's cloud and convection parameterizations, not used in the runs presented here, lead to an improvement in the simulated Indian precipitation rate. Further discussion will be given elsewhere. The simulated precipitation rate is generally larger than observed in both the control and the experiment.

Figure 11 shows the effects of the introduction of SiB2 on the simulated excess of precipitation over evaporation, which in a time average is equal to the moisture convergence (the GCM conserves moisture to machine precision). For July especially, increases

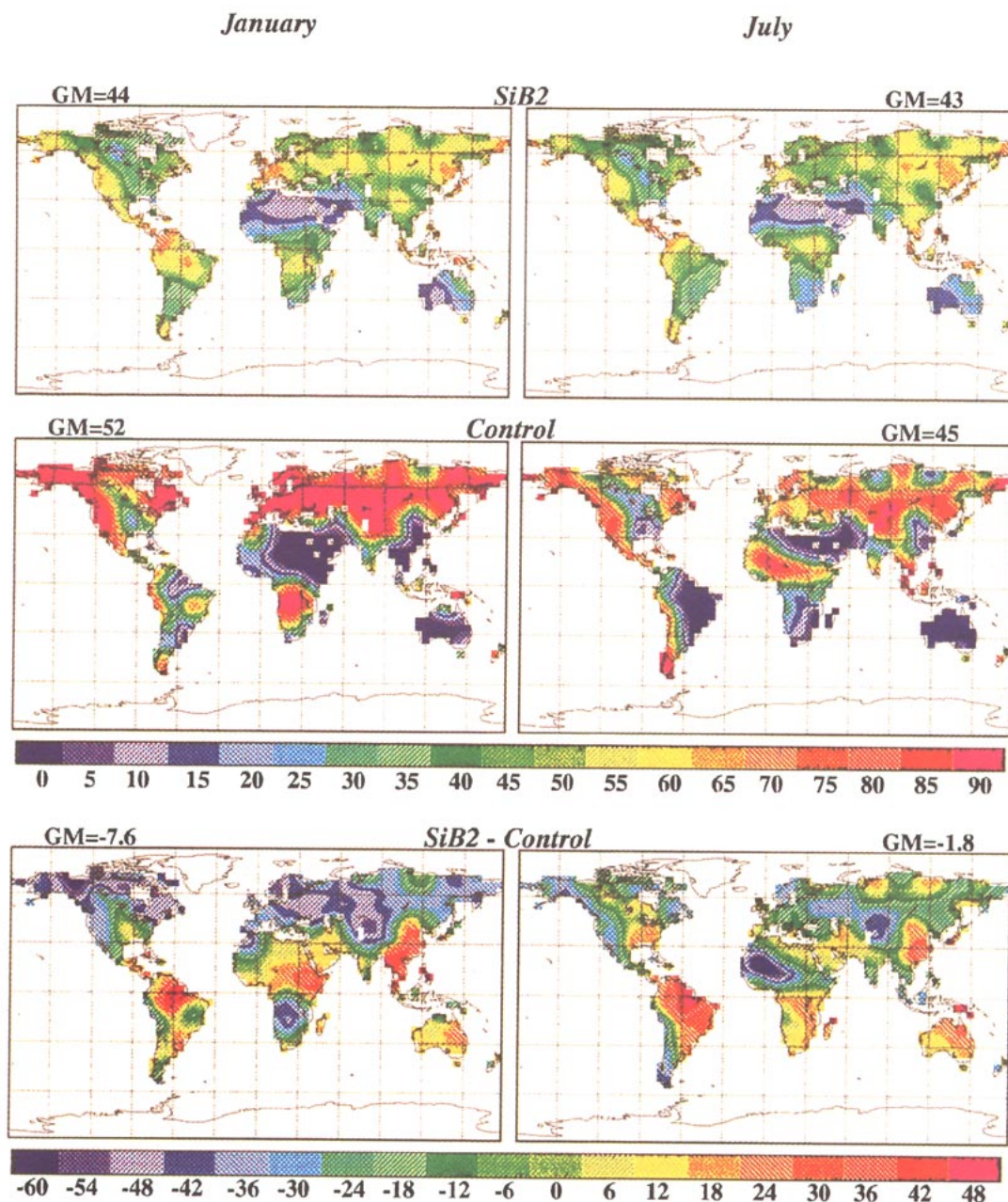


FIG. 13. Maps of the ground water as a percentage of field capacity for experiment, control, and difference for January and July.

in the precipitation rate in the SiB run relative to the control run are highly correlated with increases in the lateral moisture convergence. This is also true for the Amazon in January. Increased warmth of the continents favors stronger monsoon circulations, which import more moisture, leading to more precipitation.

Figure 12 shows the zonally averaged precipitable water (the vertically integrated water vapor content). It generally decreases over land, although it increases

in the monsoon region, especially in the Tropics. Recall from Fig. 4, however, that the surface mixing ratio decreases over nearly all continental areas, including the monsoon regions. This indicates that the increases in precipitable water in the monsoon regions are due to increases in the depth of the moist layer. We return to this below.

In the control run, the field capacity is assumed to be 15 cm of water, at all land points. The field capacity in the experiment varies geographically, as shown in

Fig. 1, and is much greater than 15 cm in many places. It is not obvious how to compare the simulated soil moisture between the two runs since the field capacities are so different. We choose to show the changes in ground water as a percent of field capacity, that is, the "normalized ground wetness"; this is presented in Fig. 13. The impact of SiB2 is that the normalized ground wetness increases in the Amazon, eastern North America, and Southeast Asia and Australia throughout the year. It decreases in eastern Europe, most of northern Asia, and western North America throughout the year. In southern Africa and western Europe, the normalized ground wetness increases in July and decreases in January relative to the control. Note, however, that the "moisture availability function," which is defined as the ratio of the actual evapotranspiration to the potential evapotranspiration, is not necessarily similar between the SiB2 run and the control. Because of this, it is not straightforward to determine, for example, to what extent the change (between the two runs) in the humidity of the air over the continents might be attributable to a change in the soil moisture as a fraction of the soil's holding capacity. It is not even clear that a simple relationship of any kind should exist between these two fields.

Figure 14 shows the time series of the globally averaged soil moisture in the second and third layers of soil in the SiB2 run, that is, the root zone and the deep moisture store, as well as the soil moisture in the bucket of the control run. The SiB2 results show weak drying trends that are gradually leveling off by the end of ten simulated years. The control run is steady (apart from the obvious seasonal cycle).

Figure 15 shows how SiB2 has affected the maximum PBL depth attained in a daily cycle, as averaged over many daily cycles. Over the oceans this average diurnal maximum is not systematically different from the simple average of the PBL depth over the entire record. With SiB2, the diurnal maximum PBL depth tends to increase in the monsoon regions and deserts, as does the average PBL turbulence kinetic energy (not shown). The maximum PBL depth also increases over Siberia in January, consistent with the warmer surface. Generally, the PBL depth increases in response to SiB2 in those places SiB2 has caused the surface sensible heat flux to increase. The daily maximum PBL depth shows a tendency to decrease, however, in some coastal regions, for example, the Caribbean in July and off the west coast of North Africa.

As shown in Fig. 16, the vertically averaged PBL wind speed also increases in many places, consistent with the greater depth of the frictional layer. Interestingly, the average PBL wind speed increases in the North Atlantic in winter, indicating stronger surface pressure gradients in that region, as will be discussed later. The increased PBL wind speed over the North Atlantic is consistent with the increased latent heat flux in that region, which has already been mentioned (see Fig. 5).

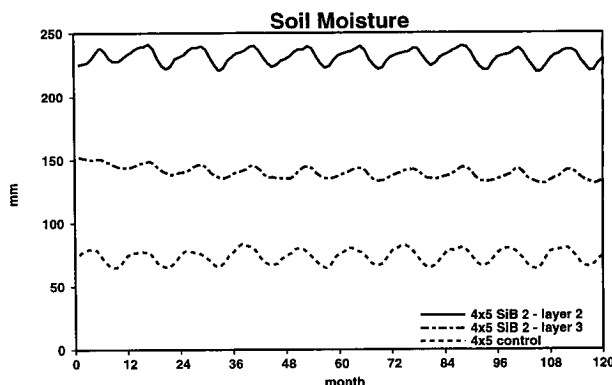


FIG. 14. Time series of the globally averaged soil moisture for layers 2 and 3 of the SiB2 run, and also for the control (units are mm of water, which is equivalent to  $\text{kg m}^{-2}$ ).

Figure 17 shows the effects of SiB2 on the simulated sea level pressure, as well as a comparison of the control sea level pressure results with ECMWF observations. The sea level pressure has decreased in most places over land, and so of course mass conservation dictates that there be a corresponding tendency for the sea level pressure to increase over the oceans. The decrease over land is to be expected in view of the surface warming discussed earlier. The strongest decreases occur over Siberia in winter, where the surface temperature has increased tremendously as already discussed. This leads to a substantial weakening and northward shift of the Siberian high, which is a change for the worse. The decreased sea level pressure is also quite noticeable over southern Asia in July. This would be expected to enhance the monsoon circulation in Southeast Asia. As already noted, the precipitation rate increases in Southeast Asia in July. The sea level pressure decreases over the North Atlantic in January. This corresponds to a deepening of the Icelandic low. The implied stronger PBL winds can be seen in Fig. 16 and are responsible for the increased latent heat flux over the North Atlantic in January, as seen in Fig. 11. The precipitation rate has also increased somewhat in the North Atlantic in January (Fig. 10).

Figure 18 shows the corresponding results for the height of the 200-mb surface. There is a general tendency for the heights to increase, especially over land, which is hydrostatically consistent with the general warming already noted. Note, however, that the 200-mb heights decrease slightly in the high latitudes of the Northern Hemisphere in January. This decrease is actually most pronounced over the North Atlantic and Eastern North America (not shown). Recall from Fig. 17 that the sea level pressure decreases in the same part of the world. Apparently SiB2 has led to an increase in storminess in the North Atlantic. The reasons for this are not obvious and are undergoing further study.

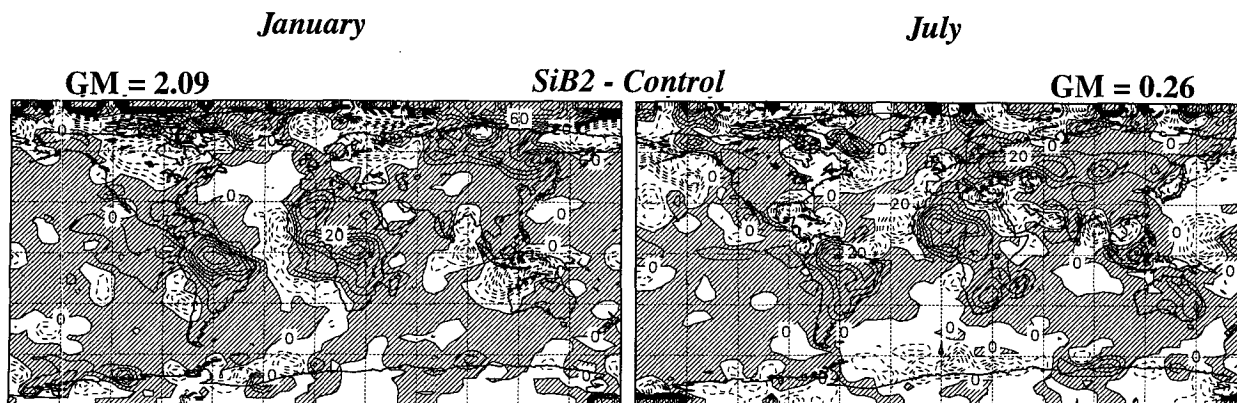


FIG. 15. Maps of the difference between the SiB2 run and the control for the maximum PBL depth attained in a daily cycle averaged over many daily cycles for January and July. The contour interval is 10 mb.

Figure 19 gives latitude–height plots of the effects of SiB2 on the zonally averaged temperature, as well as a comparison of the control run with observations. The figure makes it clear that the warming effects of SiB2 are quite widespread but are mainly confined to the lower troposphere in the Northern Hemisphere in July. In particular, the strong winter Siberian warming of the SiB2 run relative to the control is confined to a shallow layer near the earth's surface. We have examined the changes in the zonally averaged water vapor mixing ratio as a function of latitude and height and find that SiB2 has little effect on this field. Figure 20 shows latitude–height plots of the effects of SiB2 on the zonally averaged zonal wind, and also a comparison of the control run with observations. SiB2 tends to make the tropical zonal winds more easterly or less westerly. This is an improvement. SiB2 also increases the westerlies near 70°N in winter. We have looked for systematic changes in the simulated mean meridional circulation, in response to the introduction of SiB2, and have found nothing worth commenting on.

### c. Simulation of the carbon budget of the land surface by SiB2

Figure 21 shows the simulated carbon assimilation rate for January, July, and the annual mean, as calculated by the methods described in Part I. The annual mean assimilation rate of  $2.03 \text{ g m}^{-2} \text{ s}^{-1}$  at land points gives a global total assimilation of  $114 \times 10^{15} \text{ g C yr}^{-1}$  ( $114 \text{ Gt C yr}^{-1}$ ). The annual sum of net assimilation calculated by SiB reflects total leaf photosynthesis minus leaf respiration only; no representation is made of respiration in roots or stems. This quantity is impossible to measure at large spatial scales, so the realism of the estimate is unknown. A more commonly used measure of carbon fixation is the net primary production (NPP), which is defined as gross photosynthesis minus plant respiration, but this quantity is not calculated in

SiB2. A common “rule of thumb” used by ecologists (e.g., Bolin et al. 1979) states that NPP is about one-half of gross photosynthesis. Recent estimates of global NPP by Melillo et al. (1993) and Potter et al. (1993) of  $53.1 \text{ Gt C yr}^{-1}$  and  $48 \text{ Gt C yr}^{-1}$ , respectively, are nearly one-half of the net assimilation estimated by SiB2, so the SiB2 estimate appears to be quite reasonable. The geographic distribution of the annual total net assimilation in the lower panel of Fig. 21 is very similar to that produced by the models of Melillo et al. (1993) and Potter et al. (1993).

Although much of the annual net assimilation occurs in the Tropics, the northern temperate and boreal zones are regions of strong net assimilation during the growing season, as expected. The seasonal changes in carbon uptake are quite dramatic, with the northern temperate and tropical regions almost 180° out of phase. In temperature and boreal regions, the assimilation rate is near zero in January but increases to between 4 and  $9 \text{ g m}^{-2} \text{ day}^{-1}$  in July. In the tropical rainforests, the monthly mean net assimilation is as high as  $13 \text{ g m}^{-2} \text{ day}^{-1}$  in January but drops to much lower values in July as the seasonal rains move north.

On an annual basis, the assimilation of carbon by photosynthesis in nature is largely balanced by soil microbial respiration that releases  $\text{CO}_2$  to the atmosphere, but seasonal changes in plant photosynthesis and soil respiration are largely responsible for the seasonal oscillations observed in atmospheric  $\text{CO}_2$  concentration (Keeling et al. 1989; Tans et al. 1990). We have used the results shown in Fig. 21 to perform an evaluation of the surface carbon budget as simulated by the model. The surface flux of  $\text{CO}_2$  is equal to the net ecosystem production (NEP) and is calculated as

$$\text{NEP} = R - A_n, \quad (1)$$

where  $R$  is the release of  $\text{CO}_2$  from soils due to respiration (including respiration by both plant roots and soil microbes) and  $A_n$  is the net assimilation due to

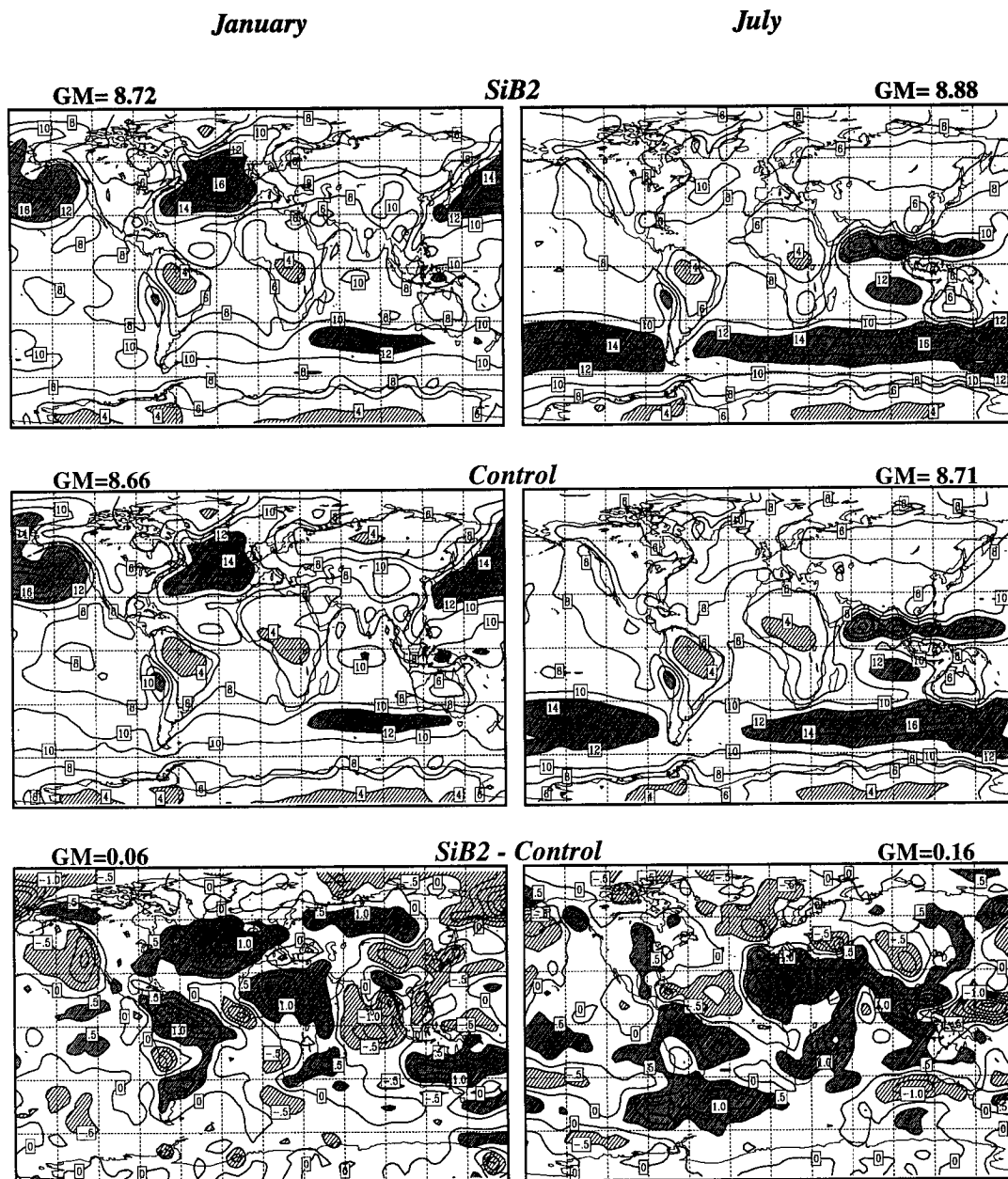


FIG. 16. Maps of the vertically averaged PBL wind speed for the SiB2 run, the control, and their difference for January and July. The contour interval is  $2 \text{ m s}^{-1}$ .

photosynthesis. It is  $A_n$  that is shown in Fig. 21. In order to evaluate the surface carbon budget, we need to determine the respiration rate. SiB2 does not include a parameterization of soil respiration, although one is under development. In the present study, we use a simple diagnostic method to determine the soil respiration rate after the model run has been completed.

The relative intensity of soil respiration, denoted by  $R^*$ , is diagnosed from soil moisture and soil temperature at each model time step following the method used by

Raich et al. (1991) in the Terrestrial Ecosystem Model. The soil respiration diagnostic,  $R^*$ , is defined as

$$R^* = 2.0^{Q_t} f(M), \quad (2)$$

where

$$f(M) = 0.2 + w_{\text{sat}}^B$$

$$B = \left( \frac{w_m^{z_m} - w_{\text{opt}}^{z_m}}{w_{\text{opt}}^{z_m} - 100^{z_m}} \right)^2. \quad (3)$$



January

July

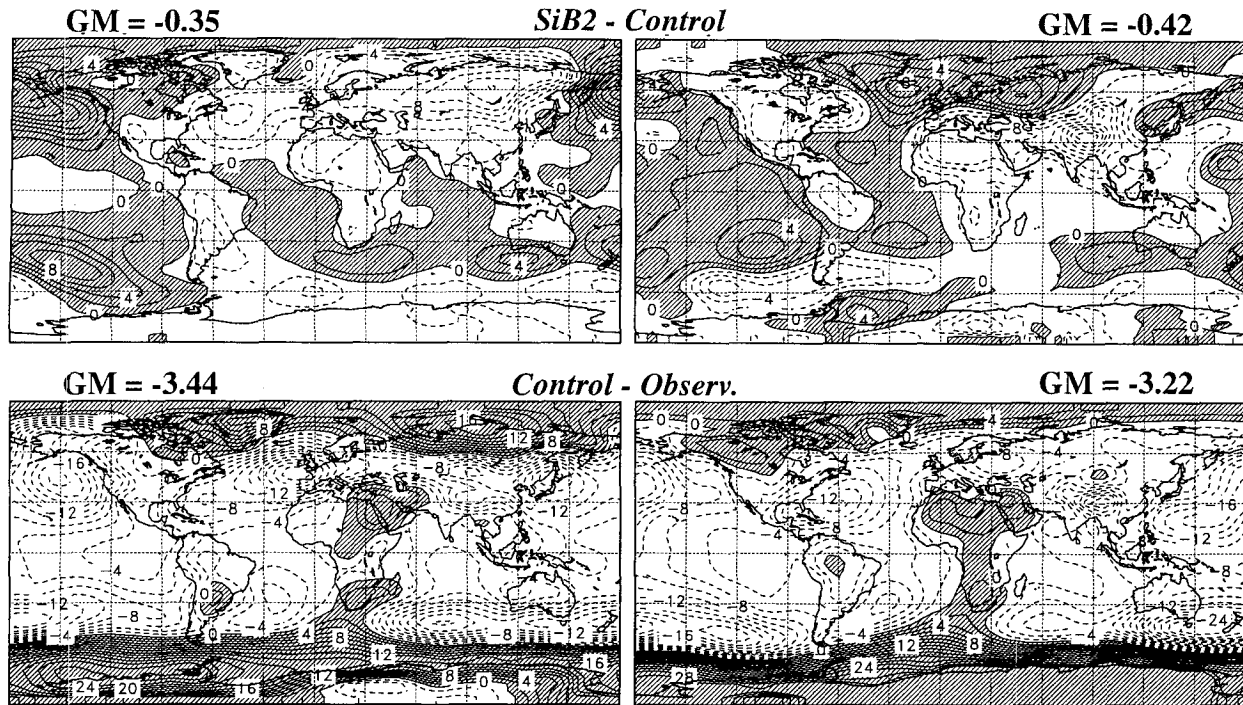


FIG. 17. Maps of the difference between the SiB2 run and the control and between the control and ECMWF observations for the simulated sea level pressure for January and July. The contour interval is 2 mb.

The temperature response function uses the same  $Q_i = (T - 298)/10$  as is used elsewhere in SiB2 (see Part I). The temperature used to define  $Q_i$  in (2) is the warmer of the surface soil temperature and the deep soil temperature. The variable  $w$  in (3) is the fraction of the pore space occupied by water in the root zone (midlayer) of the soil. The parameters  $w_{\text{sat}}$ ,  $w_{\text{opt}}$ , and  $z_m$  are prescribed according to soil texture using values suggested by Raich et al. (1991). Soil respiration is a maximum for some value  $w_{\text{opt}}$  of soil moisture, and respiration is less efficient under very dry or very wet conditions.

A dimensionless monthly mean soil respiration rate is defined as

$$\bar{r}(t) = \frac{\bar{R}^*(t)}{\sum_{1\text{year}} \bar{R}^*(t) \Delta t}, \quad (4)$$

where the overbar indicates the monthly mean. The flux of  $\text{CO}_2$  from the soil due to respiration is computed from this dimensionless rate by assuming a local steady state for carbon storage in terrestrial ecosystems on an annual basis, that is, that the annual sum of respiration loss is equal to the annual net carbon assimilation (ANA) defined as

$$\text{ANA} = \sum_{1\text{year}} \bar{A}_n(t) \Delta t, \quad (5)$$

where  $\bar{A}_n(t)$  is the monthly mean net assimilation. The flux of  $\text{CO}_2$  from the ecosystem due to respiration is calculated from  $\bar{r}(t)$  according to

$$\bar{R}(t) = \bar{r}(t) \times \text{ANA}, \quad (6)$$

so that the net annual flux of  $\text{CO}_2$  from every grid point is zero.

Figure 22 compares the seasonal patterns of the zonal sum of NEP, as represented by SiB2 and as calculated from the data of Fung et al. (1987), which produced good agreement with observed  $\text{CO}_2$  concentrations when coupled with a tracer transport model. Like the SiB2 estimates, the Fung et al. (1987) fluxes integrate to zero at every grid point on an annual basis. The contoured values represent the total flux of carbon into the atmosphere from each  $4^\circ$  latitude band in the model at a given time. The overall structure of the annual cycles is quite similar between the two estimates, with strongly seasonal fluxes in the northern midlatitudes due to the seasonal growth and decay of vegetation there. In the Tropics, the annual cycle is driven by the seasonal migration of tropical precipitation over land, with net uptake in the rainy season and net release of  $\text{CO}_2$  in the dry season.

Net release of  $\text{CO}_2$  from temperate and boreal ecosystems in the Fung et al. (1987) fluxes is confined

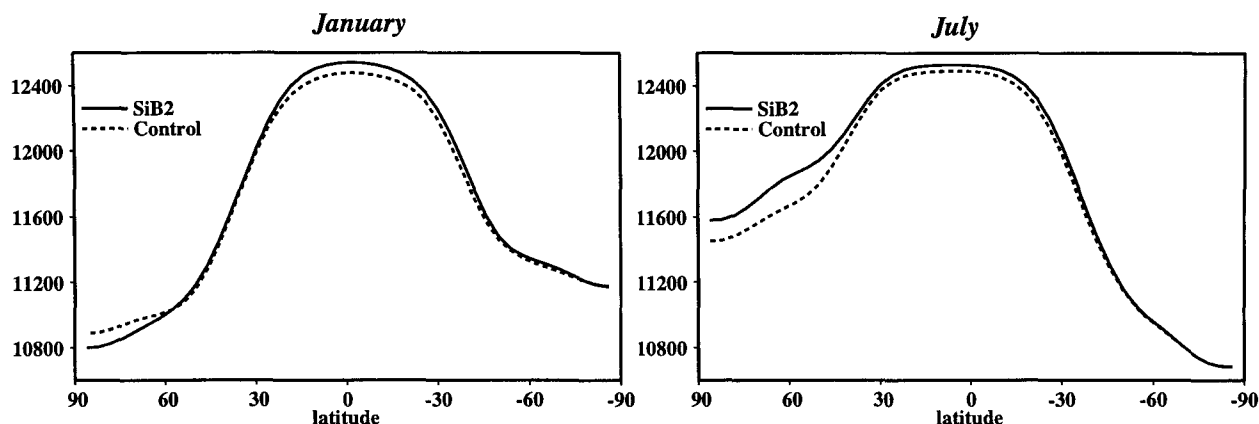


FIG. 18. The simulated zonally averaged 200-mb height for January and July for the SiB2 run and the control.

to the spring and fall seasons but extends throughout the winter as simulated by SiB2. This is due to the fact that the earlier estimates used climatological surface air temperature to drive the respiration calculation, whereas SiB2 uses the simulated *soil* temperature, which is much warmer in winter. This effect

leads to a smaller amplitude of the annual cycle of NEP in this region as simulated by SiB2. The seasonal uptake during the temperate growing season also begins about one month earlier in SiB2 than in the earlier estimates and is well established by the end of May. This is a time when the observed  $\text{CO}_2$

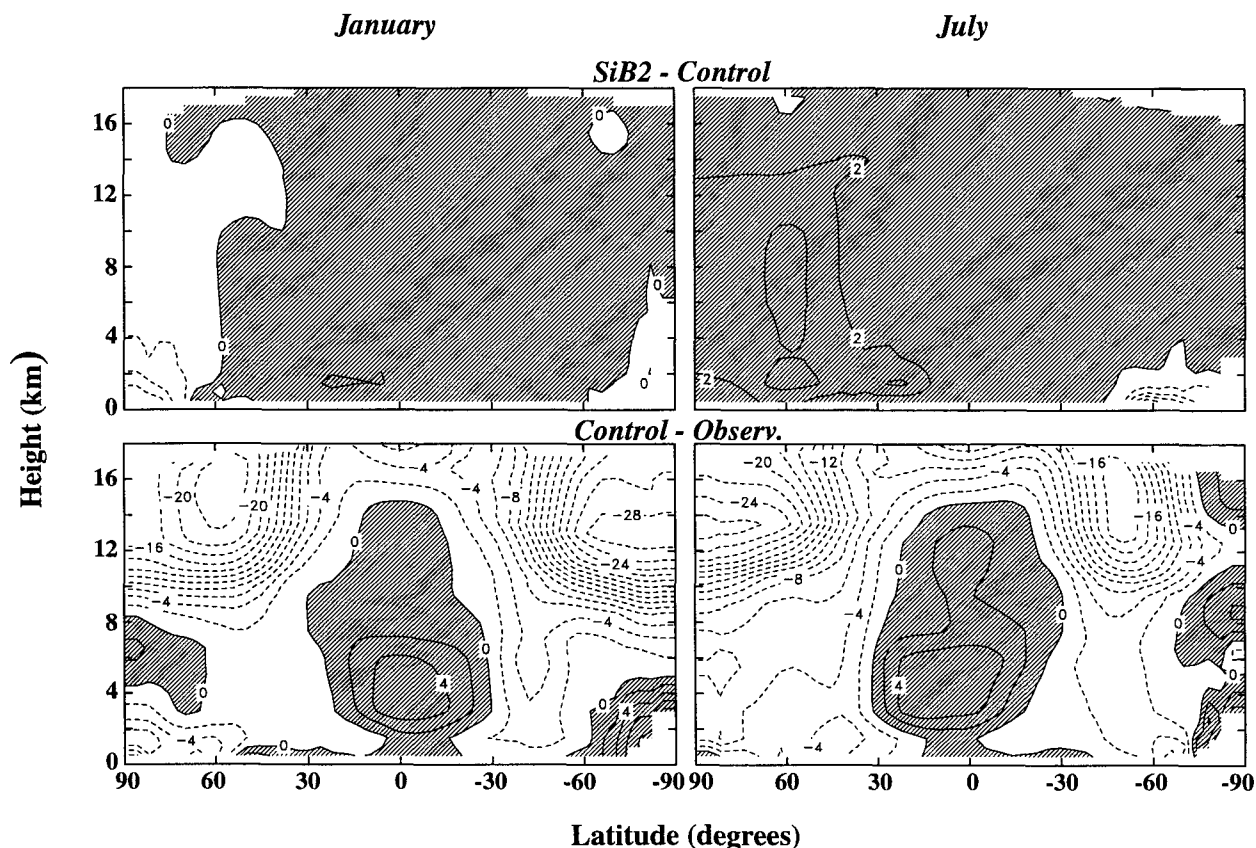


FIG. 19. Latitude-height plot of the simulated zonally averaged temperature for the difference between the SiB2 run and the control and the difference between the control and ECMWF observations. The contour interval is 2 K.

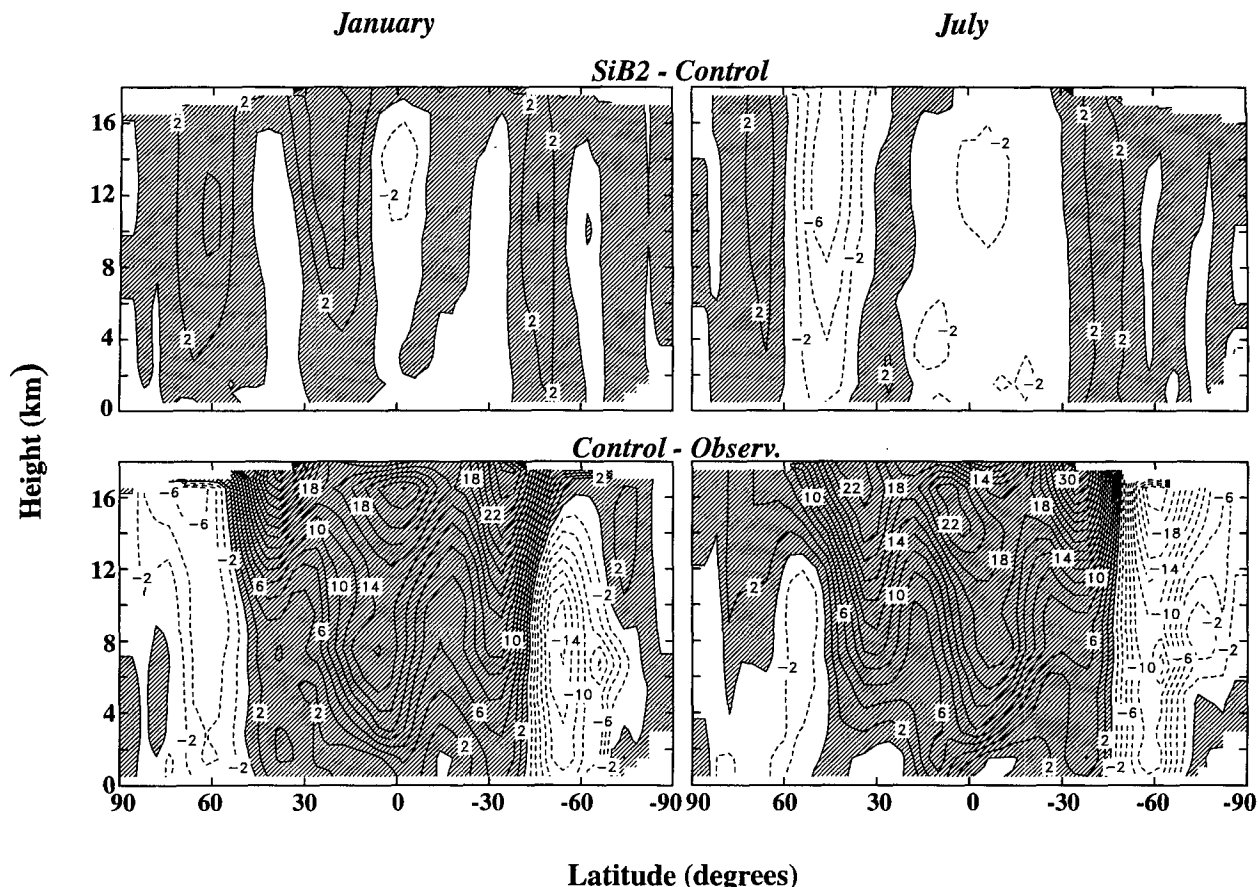


FIG. 20. Latitude–height plot of the simulated zonally averaged zonal wind for the difference between the SiB2 run and the control and the difference between the control and ECMWF observations. The contour interval is  $2 \text{ m s}^{-1}$ .

concentrations in this region are declining rapidly (Keeling et al. 1989), so the SiB2 estimate may be more realistic in this respect.

The seasonal amplitude of NEP is much stronger in the Tropics as simulated by SiB2 than as estimated by Fung et al. (1987). Much of the difference between the tropical fluxes calculated by the two methods occurs in Africa, although this cannot be seen in Fig. 22 due to the zonal averaging. The differences are especially strong in the tropical and subtropical grasslands (biome 6), which are occupied by  $C_4$  plants. The difference may be due to the different parameterization of assimilation in  $C_4$  ecosystems (Collatz et al. 1992; also see Part I), although there are virtually no measurements of  $\text{CO}_2$  in that region, so whether or not this result is realistic is unknown.

#### d. Diurnal behavior at selected points

We now present some examples of representative diurnal cycles produced by the model; see Randall et al. (1991) for a discussion of the diurnal cycle simulated by an earlier version of the same GCM. Three grid cells and

corresponding months have been chosen for discussion here: an “Amazon” basin grid cell in January, a “FIFE” grid cell in central North America for July, and a “BOREAS” grid cell in northern North America in July. (The names “FIFE” and “BOREAS” should not be taken too literally, of course, since the model grid cells studied here represent hundreds of thousands of square kilometers each.) The results presented in Fig. 23 are based on composite diurnal cycles, as averaged over the ten realizations of the particular month over the ten annual cycles of our run. Each curve plotted as a function of local time therefore represents an average or composite over 310 realizations. For each site, the variables shown are the solar radiation absorbed by the surface, the net surface energy flux, the sensible heat flux, the latent heat flux, the total precipitation rate, the surface air temperature, the PBL depth, the aerodynamic resistance, the net assimilation rate, and the stomatal conductance. These hourly results are saved for a few dozen grid points; the volume of data involved is too large to allow such detail to be saved globally.

Among the three grid cells and months considered here, the largest values of the absorbed solar radiation

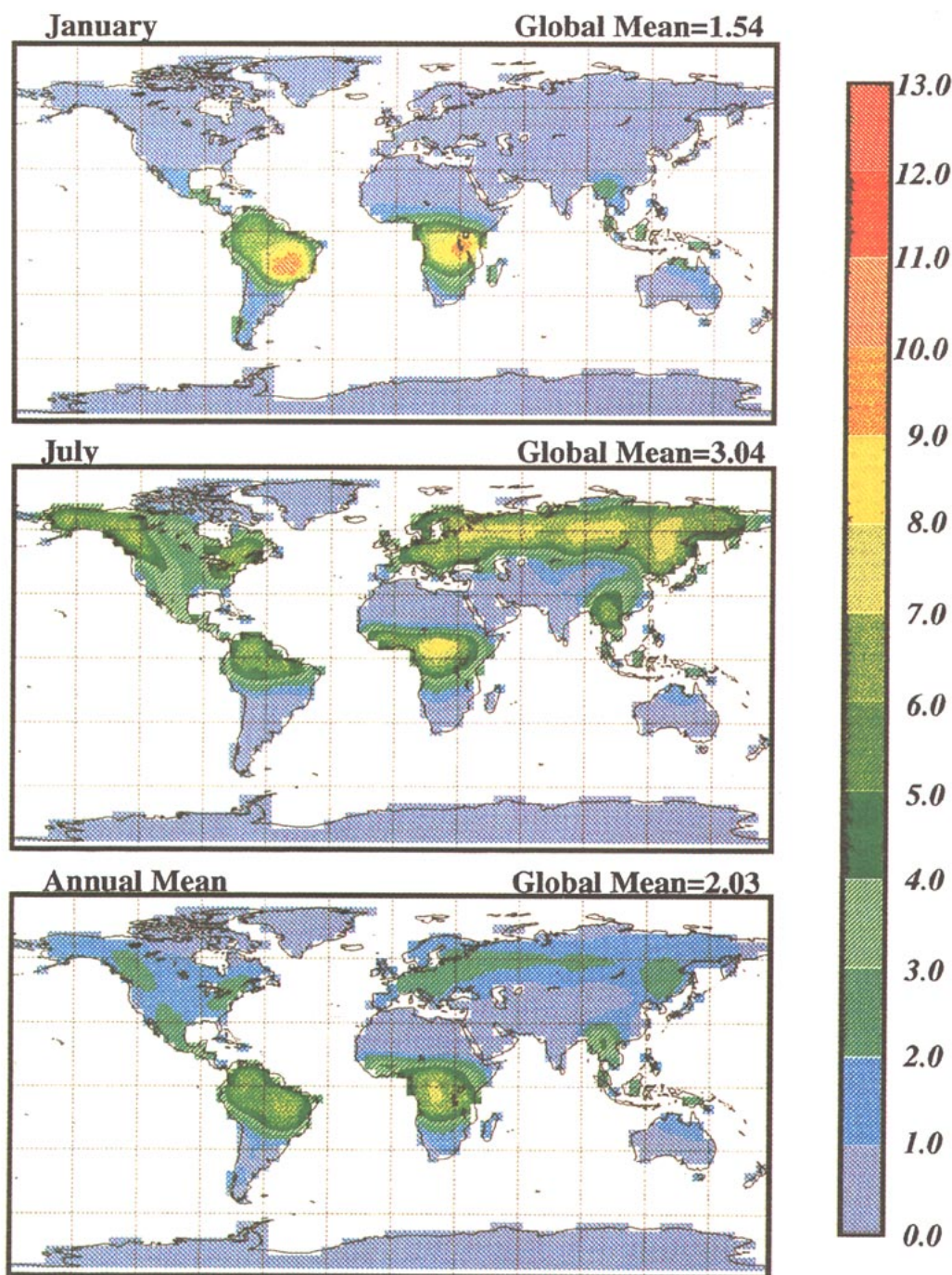


FIG. 21. Maps of the carbon assimilation rate obtained in the SiB2 run for January, July, and the annual mean. The units are  $\text{g-carbon m}^{-2} \text{ day}^{-1}$ .

and net surface energy flux occur in the FIFE region in July. Note that the points with the largest sensible heat flux are those with the lowest latent heat flux, and vice versa. The most positive values of the net surface energy flux occur near noon, before the maximum of solar radiation. The most negative values of the net surface

energy flux occur during the early evening. The daily mean of the net surface energy flux is close to zero in each case.

The precipitation rate is strongly diurnal, with a late afternoon–evening maximum at each site, especially in the Amazon. Only the Amazon has significant noc-



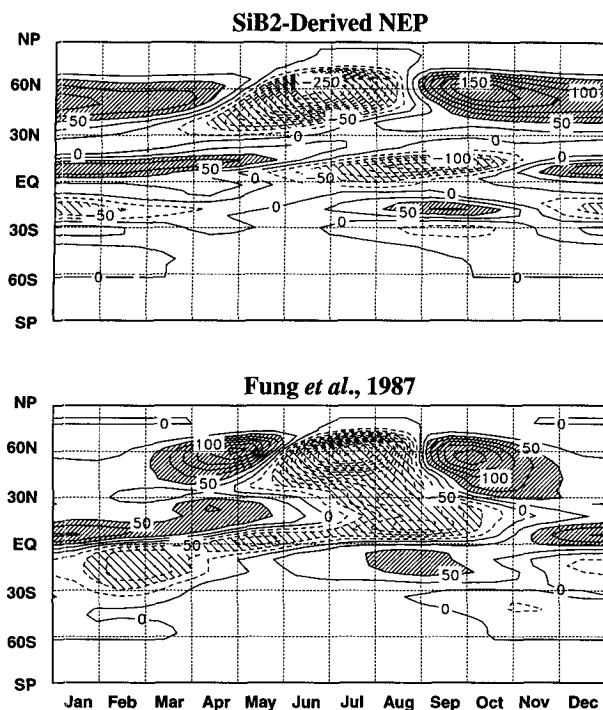


FIG. 22. The seasonal patterns of the zonally averaged uptake and release of  $\text{CO}_2$  by the terrestrial biosphere as represented by SiB and an earlier estimate (Fung et al. 1987). The contour interval is  $25 \times 10^9 \text{ kg C mo}^{-1} \text{ per } 4^\circ \text{ latitude bin}$ . Values larger than 50 are shaded, and those less than  $-50$  are hatched.

turnal precipitation. There is a weak afternoon minimum of the precipitation rate at all three sites; the significance of this is unknown, but it may be related to an afternoon minimum of the stomatal conductance, discussed below.

The surface air temperature is of course also strongly diurnal, with the highest maximum at the FIFE site, reaching about 308 K near 1400 local time. The Amazon cools relatively little at night due to high humidities and nocturnal cloudiness.

The PBL depth undergoes strong and very orderly diurnal progression, reaching its highest afternoon maximum at the BOREAS site and its lowest afternoon maximum at the Amazon site. In the Amazon, afternoon cumulus convection drains mass from the PBL and so limits its depth. The diurnal range of the PBL depth is smallest in the Amazon. At all three sites, the aerodynamic resistance reaches its largest values around sunset and has a fairly flat minimum during the day.

The net assimilation rate is by far the largest in the Amazon. At the FIFE site it shows an afternoon minimum. This is associated with an afternoon minimum of the stomatal conductance caused by afternoon temperature stress. Somewhat similar behavior can be seen at the Amazon and BOREAS grid cells. The small negative nocturnal assimilation rates represent leaf respiration.

## 5. Summary and conclusions

We have successfully tested SiB2 in the Colorado State University General Circulation Model. We now consider SiB2 to be an operational, “standard” component of the model, rather than an experimental appendage.

Successes of SiB2 include a realistic simulation of the rate of carbon assimilation by land–surface vegetation, a more realistic simulation of the surface air temperature, and an improved simulation of the hydrologic cycle. Some of these changes, for example, the warmer, drier boundary layer in the Tropics and summer mid-latitudes, with more surface sensible heat flux and less evapotranspiration, arise from the biophysical parameterization of evapotranspiration in terms of stomatal closure as linked to photosynthesis (see Part I). Other changes in the model results arise from more straightforward changes in the model, for example, the warming in the Siberian winter, which is primarily due to the increase in the heat capacity of the soil.

The new version of the model predicts the spatially and temporally varying rate of carbon fixation by photosynthesis. This is perhaps the most important change in the model. It represents a “hook” that can be used to couple the atmospheric model with the terrestrial component of the carbon cycle. We are actively pursuing this option at the present time.

At present, SiB2 coupled with the GCM can be used to explore the effects of interannual and intra-annual vegetation changes on regional climate and carbon fluxes; this can be done for real cases over the period 1982–1990, for which we have NDVI data. More interestingly, as the photosynthesis–conductance model in SiB2 is directly responsive to changes in  $\text{CO}_2$ , the model can also be used to explore the continental-scale physiological response to increasing atmospheric  $\text{CO}_2$  concentrations, which can be expected to lead to reduced evapotranspiration rates.

Denning and Randall (1993) have added prognostic carbon dioxide to the GCM, with prescribed distributions of surface sources and sinks, and has demonstrated that the model can reproduce the observed seasonal cycle of the spatial distribution of  $\text{CO}_2$ .

When we began this work, the primary goal was to improve the simulations of surface temperature and humidity and the fluxes of sensible and latent heat. Our perspective has evolved. We now see simulation of the terrestrial component of the carbon cycle as the most important element of SiB. We plan to develop this element further in the near future.

Future plans include:

- tests of SiB2 in other GCMs, and perhaps also in mesoscale models;
- sensitivity studies designed to take advantage of SiB’s coupling of the hydrologic cycle with photosynthesis;



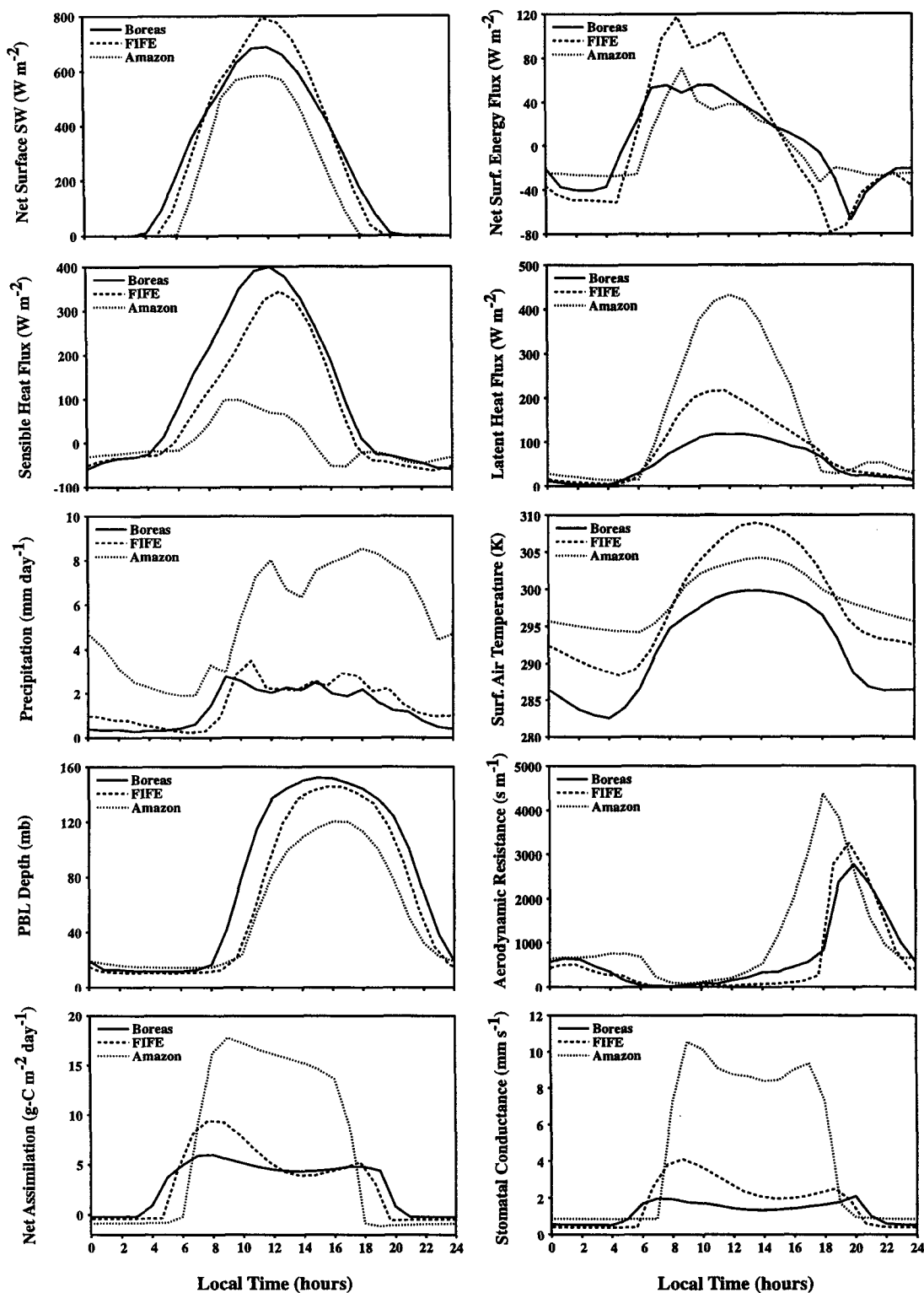


FIG. 23. Composite diurnal cycles of the solar radiation absorbed by the surface, the net surface energy flux, the sensible heat flux, the latent heat flux, the total precipitation rate, the surface air temperature, the PBL depth, the aerodynamic resistance, the net assimilation rate, and the stomatal conductance for the Amazon in January (dotted curves), FIFE in July (dashed curves), and BOREAS in July (solid curves).

- tests in which the one-dimensional version of SiB2 is driven with ECMWF analyses, rather than by the GCM;

- “boundary anomaly” experiments in which the GCM is driven with observed NDVI anomalies for real years to investigate the extent to which observed inter-annual weather anomalies can be reproduced;

- extension of SiB to include respiration from litter and soil, thus allowing a more complete simulation of the terrestrial component of the carbon cycle;

- incorporation of improved models of the soil and of the snow;

- development of an improved parameterization of boundary-layer turbulence, as it effects the surface fluxes, the entrainment rate, and the vertical distribution of the mean potential temperature, water vapor mixing ratio, and wind components through the depth of the PBL;

- extending SiB to include prognostic biomass.

These challenging projects will require several years to complete, but the present study represents a first step toward achieving that goal.

**Acknowledgments.** Support for this project was provided by NASA Earth Observing System (EOS) funds through the Sellers-Mooney Interdisciplinary Science Project. Additional support was provided by the CHAMMP Program of the Department of Energy under Grant number DE-FG02-91ER61218 to Colorado State University and by subcontract 0965G4A007 from the University of California, Los Angeles, funds provided by NASA Grant NAG 5-2224 to UCLA.

Computing resources were provided by the NCCS of the Goddard Space Flight Center, and by NERSC at the Lawrence Livermore National Laboratory.

The late T. G. Corsetti provided programming support at an early stage of the project.

#### REFERENCES

- Arakawa, A., and W. H. Schubert, 1974: The interaction of a cumulus cloud ensemble with the large-scale environment. Part I. *J. Atmos. Sci.*, **31**, 674–701.
- , and V. R. Lamb, 1977: Computational design of the basic dynamical processes of the UCLA general circulation model. *Methods in Computational Physics*, Vol. 17, Academic Press, 173–265.
- , and —, 1981: A potential enstrophy and energy conserving scheme for the shallow water equations. *Mon. Wea. Rev.*, **109**, 18–36.
- Bolin, B., E. T. Degens, P. Duvigneaud, and S. Kempe, 1979: The global biogeochemical carbon cycle. *The Global Carbon Cycle: SCOPE 13*, B. Bolin, E. T. Degens, S. Kempe, and P. Ketner, Eds., Wiley, 1–53.
- Collatz, G. J., M. Ribas-Carbo, and J. A. Berry, 1992: Coupled photosynthesis-stomatal conductance model for leaves of C4 plants. *Aust. J. Plant Physiol.*, **19**, 519–538.
- Deardorff, J. W., 1977: Efficient prediction of ground surface temperature and moisture, with inclusion of a layer of vegetation. *J. Geophys. Res.*, **83**, 1889–1903.
- Denning, A. S., and D. A. Randall, 1993: Investigation of the global carbon cycle using an atmospheric general circulation model. *Fall 1993 AGU Meeting*, San Francisco, CA.
- Dickinson, R. E., 1983: Land surface processes and climate-surface albedos and energy balance. *Adv. Geophys.*, **25**, 305–353.
- , A. Henderson-Sellers, P. J. Kennedy, and M. F. Wilson, 1986: Biosphere-atmosphere transfer scheme (BATS) for the NCAR Community Climate Model. NCAR Tech. Note, NCAR/TN-275+STR, National Center for Atmospheric Research, Boulder CO, 69 pp.
- Fowler, L. D., D. A. Randall, and S. A. Rutledge, 1996: Liquid and ice cloud microphysics in the CSU general circulation model. Part 1: Model description and simulated microphysical processes. *J. Climate*, **9**, 489–529.
- Fung, I. Y., C. J. Tucker, and K. C. Prentice, 1987: Application of advanced very high resolution radiometer vegetation index to study atmosphere-biosphere exchange of CO<sub>2</sub>. *J. Geophys. Res.*, **92**, 2999–3015.
- Garratt, J. R., 1993: Sensitivity of climate simulations to land-surface and atmospheric boundary-layer treatments—a review. *J. Climate*, **6**, 419–449.
- Harshvardhan, R. Davies, D. A. Randall, and T. G. Corsetti, 1987: A fast radiation parameterization for general circulation models. *J. Geophys. Res.*, **92**, 1009–1016.
- , D. A. Randall, T. G. Corsetti, and D. A. Dazlich, 1989: Earth radiation budget and cloudiness simulations with a general circulation model. *J. Atmos. Sci.*, **46**, 1922–1942.
- Kalnay, E., and M. Kanamitsu, 1988: Time schemes for strongly nonlinear damping equations. *Mon. Wea. Rev.*, **116**, 1945–1958.
- Keeling, C. D., R. B. Bacastow, A. F. Carter, S. C. Piper, T. P. Whorf, M. Heimann, W. G. Mook, and H. Roeloffzen, 1989: A three-dimensional model of atmospheric CO<sub>2</sub> transport based on observed winds. Part 1: Analysis of observational data. *Aspects of Climate Variability in the Pacific and Western Americas, Geophys. Monogr. No. 55*, Amer. Geophys. Union, 165–236.
- Legates, D. R., and C. J. Willmott, 1990a: Mean seasonal and spatial variability in global surface air temperature. *Theor. Appl. Climatol.*, **40**, 11–21.
- , and —, 1990b: Mean seasonal and spatial variability in gauge-corrected global precipitation. *Int. J. Climatol.*, **10**, 111–127.
- Lord, S. J., W. C. Chao, and A. Arakawa, 1982: Interaction of a cumulus cloud ensemble with the large-scale environment. Part IV: The discrete model. *J. Atmos. Sci.*, **39**, 104–113.
- Melillo, J. M., A. D. McGuire, D. W. Kicklighter, B. Moore III, C. J. Vorosmarty, and A. L. Schloss, 1993: Global climate change and terrestrial net primary productivity. *Nature*, **363**, 234–240.
- Milly, P. C. D., and K. A. Dunne, 1994: Sensitivity of the global water cycle to the water-holding capacity of land. *J. Climate*, **7**, 506–526.
- Mintz, Y., 1984: The sensitivity of numerically simulated climates to land surface boundary conditions. *The Global Climate*, J. T. Houghton, Ed., Cambridge University Press, 70–105.
- Payne, R. E., 1972: Albedo of the sea surface. *J. Atmos. Sci.*, **29**, 959–970.
- Potter, C. S., J. T. Randerson, C. B. Field, P. A. Matson, P. M. Vitousek, H. A. Mooney, and S. A. Klooster, 1993: Terrestrial ecosystem production: A process-oriented model based on global satellite and surface data. *Global Biogeochem. Cyc.*, **7**, 811–842.
- Raich, J. W., E. B. Rastetter, J. M. Melillo, D. W. Kicklighter, P. A. Steudler, and B. J. Peterson, 1991: Potential net primary productivity of South America: Application of a global model. *Ecol. Application*, **1**, 399–429.
- Randall, D. A., 1980: Entrainment into a stratocumulus layer with distributed radiative cooling. *J. Atmos. Sci.*, **37**, 148–159.
- , 1984: Buoyant production and consumption of turbulence kinetic energy in cloud-topped mixed layers. *J. Atmos. Sci.*, **41**, 402–413.
- , and D.-M. Pan, 1993: Implementation of the Arakawa–Schubert cumulus parameterization with a prognostic closure. *Cumulus Parameterization, Meteor. Monogr. No. 24*, Amer. Meteor. Soc., 137–144.

- , J. A. Abeles, and T. G. Corsetti, 1985: Seasonal simulations of the planetary boundary layer and boundary-layer stratocumulus clouds with a general circulation model. *J. Atmos. Sci.*, **42**, 641–676.
- , Harshvardhan, D. A. Dazlich, and T. G. Corsetti, 1989: Interactions among radiation, convection, and large-scale dynamics in a general circulation model. *J. Atmos. Sci.*, **46**, 1943–1970.
- , ———, and ———, 1991: Diurnal variability of the hydrologic cycle in a general circulation model. *J. Atmos. Sci.*, **48**, 40–62.
- Sato, N., P. J. Sellers, D. A. Randall, E. K. Schneider, J. Shukla, J. L. Kinter III, Y.-T. Hou, and E. Albertazzi, 1989a: Effects of implementing the Simple Biosphere Model (SiB) in a general circulation model. *J. Atmos. Sci.*, **46**, 2657–2782.
- , ———, ———, ———, ———, and ———, 1989b: Implementing the Simple Biosphere Model (SiB) in a general circulation model: Methodology and results. NASA Contractor Report, NASA HQ, 70 pp. [Available from Independence Avenue, Washington D.C. 20545].
- Sellers, P. J., Y. Mintz, Y. C. Sud, and A. Dalcher, 1986: A simple biosphere model (SiB) for use within general circulation models. *J. Atmos. Sci.*, **43**, 505–531.
- , D. A. Randall, G. J. Collatz, J. Berry, C. Field, D. A. Dazlich, and C. Zhang, 1996a: A revised land-surface parameterization (SiB2) for atmospheric GCMs. Part I: Model formulation. *J. Climate*, **9**, 676–705.
- , S. O. Los, C. J. Tucker, C. O. Justice, D. A. Dazlich, G. J. Collatz, and D. A. Randall, 1996b: A revised land surface parameterization (SiB2) for atmospheric GCMs. Part II: The generation of global fields of terrestrial biophysical parameters from satellite data. *J. Climate*, **9**, 706–737.
- Stephens, G. L., D. A. Randall, S. J. Tjemkes, I. M. Wittmeyer, and D. A. Dazlich, 1993: The earth's radiation budget in relation to atmospheric hydrology cycle. Part III: Comparison of observations with a GCM. *J. Geophys. Res.*, **98**, 4931–4950.
- Suarez, M. J., A. Arakawa, and D. A. Randall, 1983: Parameterization of the planetary boundary layer in the UCLA general circulation model: Formulation and results. *Mon. Wea. Rev.*, **111**, 2224–2243.
- Tans, P. P., I. Y. Fung, and T. Takahashi, 1990: Observational constraints on the global atmospheric CO<sub>2</sub> budget. *Science*, **247**, 1431–1438.